Loss of *lrrk2* impairs dopamine catabolism, cell proliferation, and neuronal regeneration in the zebrafish brain

Stefano Suzzi[1], Reiner Ahrendt[1], Stefan Hans[1], Svetlana A. Semenova[2], Saygın Bilican[1], Shady Sayed[1], Sylke Winkler[3], Sandra Spieß[1], Jan Kaslin[1,#a], Pertti Panula[2], Michael Brand[1*]

[1]Biotechnology Center (BIOTEC) and Center for Regenerative Therapies Technische Universität Dresden (CRTD), Dresden, Germany;

[2]Neuroscience Center, Institute of Biomedicine/Anatomy, University of Helsinki, Helsinki, Finland;

[3]Max Planck Institute of Molecular Cell Biology and Genetics (MPI-CBG), Dresden, Germany;

[#a]Current Address: Australian Regenerative Medicine Institute, Monash University, Clayton, Australia

* Corresponding author, e-mail: michael.brand@tu-dresden.de

Abstract

LRRK2 mutations are a major cause of Parkinson's disease. Pathogenicity of LRRK2 loss-of-function is controversial, as knockout in rodents reportedly induces no brain-specific effects and knockdown studies in zebrafish are conflicting. Here we show that CRISPR/Cas9-engineered deletion of the ~60-kbp-long zebrafish *lrrk2* locus elicits a pleomorphic, albeit transient brain phenotype in maternal-zygotic mutants (mzLrrk2). Intriguingly, 11-month-old mzLrrk2 adults display increased dopamine and serotonin catabolism. Additionally, we find decreased mitosis in the larval brain and reduced stab injury-induced neuronal regeneration in the adult telencephalon. Finally, hypokinesia associates with loss of *lrrk2* in larvae. Our results demonstrate that *lrrk2* knockout has an early neurodevelopmental effect, and leads to perturbed dopamine and serotonin catabolism in a *LRRK2* knockout. We propose mzLrrk2 zebrafish as a valuable tool to study LRRK2 loss-of-function *in vivo*, and provide a link between LRRK2 and the control of basal cell proliferation in the brain that may become potentially critical upon challenges like brain injury.

Introduction

The leucine-rich repeat kinase 2 (LRRK2/dardarin/PARK8) is a large multidomain protein and a bifunctional enzyme, displaying both kinase and GTPase activities [1]. *LRRK2* gene polymorphisms are the most recurrent genetic cause of familial and sporadic late-onset Parkinson's disease (PD) reported so far, although the relative frequency of individual mutations varies with ethnicity [2]. *LRRK2* mutations cause pleomorphic and highly variable pathology, sometimes clinically indistinguishable from late-onset levodopa-sensitive idiopathic disease [3]. Typical features include selective dopaminergic cell loss and presence of Lewy bodies, abnormal protein aggregates associated with several neurodegenerative disorders [4].

In vitro evidence has initially suggested that pathogenic variants, including the relatively common G2019S substitution, confer toxicity via gain-of-function of the kinase domain [5, 6]. As a result, LRRK2 pharmacological inhibition attracts great interest in a therapeutic perspective. However, a loss-of-function contribution has not been ruled out. First, the current lack of reliable endogenous substrates or interaction partners makes it difficult to validate *in vitro* findings *in vivo*. More critically, mice overexpressing human wild-type [7] or mutant LRRK2 [8-13] do not generally recapitulate dopaminergic cell loss, unless transgene levels are artificially enhanced using strong promoters [11, 14-17]; Lewy body pathology has never been reported. Paradoxically, enhanced LRRK2 activity in G2019S knockin mice confers a hyperkinetic phenotype and seems protective against age-related motor impairment [18]. A further challenge comes from evidence that the G2385R variant, a risk factor for PD in the Chinese ethnicity [19, 20], reduces kinase activity [21, 22] and enhances LRRK2 degradation [21]. A similar dominant negative effect has been described also for the I2020T variant [23, 24], usually considered a gain-of-function. Finally, pathogenic variants may disrupt protein-protein interactions that may be essential in cell signaling pathways. Along this line, it has been shown that the substitutions R1441C/G/H, Y1699C, and I2020T, but not G2019S, reduce phosphorylation of LRRK2 residues S910/S935 in Swiss 3T3 cells, thus disrupting the interaction with 14-3-3 protein and causing non-14-3-3 bound LRRK2 to accumulate in inclusion body-like cytosolic pools [25]. Altogether, these observations back up an alternative loss-of-function hypothesis, bolstered by *Lrrk2* knockout in rodents being pathogenic in peripheral organs [26-28]. Remarkably, *Lrrk2* knockout mice develop PD-like pathology in the kidney, most prominently accumulation and aggregation of α-synuclein, but not in the brain [28]. Yet, LRRK2 deficiency in mice induces behavioral alterations similar to BAC human LRRK2 G2019S transgenic mice [29, 30].

These data emphasize the importance of additional knockout studies to elucidate LRRK2 function. *LRRK2* knockout models may help clarifying the molecular interactions that are disrupted by dysfunctional LRRK2, as well as potential side effects of LRRK2 inhibitors. The zebrafish is a valuable addition to rodent models due to its amenability to high-throughput studies and direct observation of disease mechanisms *in vivo*. In particular, the regenerative potential of the zebrafish adult brain [31] makes it a useful vertebrate system to determine which genetic programs might hinder neurodegeneration, with a view towards applying these insights in humans. Previous attempts to investigate zebrafish *lrrk2* gene function using morpholino oligonucleotides (MOs) yielded contradicting results. In one study, loss of diencephalic catecholaminergic (CA) neurons and locomotor defects in the larvae were described [32]. However, a subsequent study failed to reproduce the reported phenotype, even by using the same reagents and MOs [33]. Recently, a third paper rekindled the initial claims, describing a *lrrk2* MO-induced phenotype with strong developmental abnormalities [34]. These discrepancies revived concerns over the consistency of MO-induced knockdown to assess gene loss-of-function due to the variability and transiency of induced changes and the risk of off-target effects [35]. Although the analysis of MO-induced phenotypes may still provide useful information, their validation would inevitably entail the generation of reliable null alleles [36].

Using the clustered regularly interspaced short palindromic repeats (CRISPR)/CRISPR-associated protein-9 nuclease (Cas9) genome-editing tool, we report here the deletion of the ~60-kbp-long zebrafish *lrrk2* locus containing the entire open reading frame (ORF), resulting in an unambiguous null allele. To our knowledge, this is the first report describing LRRK2 deficiency in a vertebrate *in vivo* model where no residual or truncated protein is produced. We also report a second point mutant resulting in an early stop codon as a potential null allele. We characterized the phenotype of these alleles in the brain, as the organ of possibly

highest relevance for PD. We find that maternal-zygotic *lrrk2* mutants display a pleomorphic, but transient neurodevelopmental phenotype, including increased apoptosis, delayed myelination, reduced and morphologically abnormal microglia/leukocytes, and reduced catecholaminergic neurons. We also find a correlation between hypokinesia and loss of *lrrk2* in larvae. Importantly, we also find perturbed amine catabolism in progressively older adult animals. Finally, we observe decreased mitosis in the larval brain and impaired neuronal regeneration after stabbing the adult telencephalon. Our results suggest a link between zebrafish Lrrk2 and the control of cell proliferation in the brain, with crucial implications for the self-healing capacity upon lesion.

Results

Deletion of the entire *lrrk2* locus using CRISPR/Cas9

Syntenic analysis using the assemblies of the human and zebrafish genomes (GRCh38p.7 and GRCz10, respectively) revealed the conservation of *SLC2A13* as the downstream neighbor of *LRRK2* in both species. Moreover, duplication of the zebrafish *lrrk2* locus is not reported. The human LRRK2 and zebrafish Lrrk2 proteins share the same domain structure, with the kinase domain displaying the highest degree of conservation (Figure 1a); three of the four sites of pathogenic substitutions in humans are fully conserved (Table 1). Together, these data suggest that human *LRRK2* and zebrafish *lrrk2* are truly orthologous genes.

Table 1. Sites of pathogenic amino acid substitutions in human LRRK2 and corresponding residues in zebrafish Lrrk2.

substitution in humans	corresponding site in zebrafish	protein domain
p.Arg1441Cys/Gly/His		
p.Tyr1699Cys	Tyr1685	COR
p.Gly2019Ser	Gly2009	kinase
p.Ile2020Thr	Ile2010	kinase

Data retrieved from the Parkinson Disease Mutation Database (PDmutDB, http://www.molgen.vib-ua.be/PDmutDB) [37, 38].

To study the gene function of zebrafish *lrrk2 in vivo* and potentially resolve the controversy arising from previous MO studies [32-34], we removed the *lrrk2* locus containing the entire ORF. This approach has two main advantages. First, potential side effects of frameshift mutations, including cellular stress due to aberrant transcripts or truncated protein products with residual or new function, are excluded. Second, identification of mutation carriers is straightforward. To achieve full deletion of the *lrrk2* locus, two CRISPR/Cas9 target sites flanking the 60 kb-long ORF were chosen (Figure 1b). To identify deletion alleles, a gap-PCR strategy was devised, with primers amplifying a 289-bp-long amplicon inside the target region duplexed with flanking primers, unable to direct amplification unless a deletion brings them in sufficient reciprocal proximity (Figure 1b, c). The selected founder produced offspring where the flanking primers amplified a 204-bp-long product, revealing a 60,243-bp-long targeted deletion (c.–61_*42del according to the Human Genome Variation Society guidelines [39]; henceforth this allele is referred to as "tud113") as confirmed by sequencing. The complete absence of *lrrk2* expression in homozygous tud113 mutants was verified via *in situ* hybridization (Figure 1d).

F1 heterozygous fish were incrossed to obtain F2 homozygous tud113 mutants and wild types. To exclude any effect from the existing maternal wild-type *lrrk2* transcripts (Figure S1a), F2 fish were further incrossed to obtain homozygous mutants that developed from homozygous mothers (maternal-zygotic homozygous tud113 mutants, henceforth referred to as "mzLrrk2") and wild-type (wt) control lines. In striking contrast with published MO-induced phenotypes [32, 34], mzLrrk2 individuals develop normally, are viable, and reach sexual maturity at the same age as controls, with both females and males being fertile. During

zebrafish development, *lrrk2* expression is ubiquitous until 24 hours post-fertilization (hpf), then gradually restricts to the head (Figure S1); *lrrk2* transcripts are relatively scant in whole-body 5- and 10-dpf larvae, as measured by RT-qPCR (not shown). In the adult brain, *lrrk2* expression is present throughout the whole organ (Figure S2). The time course of *lrrk2* expression in the zebrafish brain thus closely mirrors the situation in rodents, where *Lrrk2* is broadly expressed in the embryonic, postnatal, and adult brain, though at low levels compared to other peripheral tissues [40-42]. To exclude possible compensation from the paralogous *lrrk1* gene, we also characterized *lrrk1* expression in developing embryos (Figure S3a–f'). Compared to *lrrk2* (Figure S1a–i), *lrrk1* expression is markedly tissue-restricted. Moreover, *lrrk1* is not upregulated in mzLrrk2 larvae either at 5 or at 10 days post-fertilization (dpf) as determined by RT-qPCR (Figure S3g).

Pleomorphic but transient brain phenotype in mzLrrk2 fish

Because the link between *LRRK2* and PD in humans implies a critical role in brain function, we characterized mzLrrk2 fish with regard to the brain phenotype at both larval (5 and 10 dpf) and adult (6 and 11 months, mo) stages. Using TUNEL assay, we measured a threefold increase of the cell death rate in mzLrrk2 brains at 5 dpf (anterior: P=0.0061; middle: P<0.0001; Figure 2a, a'), but not at 10 dpf (Figure 2b, b'). Unlike previous studies [32, 34], no clear sign of neuronal loss was evident after HuC/D staining at either 5 or 10 dpf (Figure 2c, d). Likewise, the commissural acetylated Tubulin+ axons in the tectum appeared normal at both larval time points (Figure 2e, f). To further investigate the consequences of Lrrk2 deficiency on neural development, Claudin k staining was performed to visualize myelination. Claudin k expression was delayed in the ventromedial hindbrain of mzLrrk2 at 5 dpf (Figure 2g), but normal at 10 dpf (Figure 2h). In summary, our data show that loss of *lrrk2* causes early, but transient defects, including increased apoptosis and delayed myelination, albeit no obvious signs of neurodegeneration.

Neuroinflammation is a concurring factor in many neurodegenerative conditions, including PD [43]. Increasing evidence implicates *LRRK2* in microglia function [44]. Because the shape of microglia may be indicative of their activation state, we used the pan-leukocyte marker L-Plastin and examined the brain microglia/leukocyte number and morphology (Figure S4a). The overall number was reduced by about one third in 5-dpf mzLrrk2 larvae (Figure 3a, a'; P=0.0273). The trend was maintained until 10 dpf, though without reaching statistical significance (P=0.0797; Figure 3b, b'). For each brain, average microglia/leukocyte volume, surface, ramification, average branch length, maximum branch length, and longest shortest path were used to study the variance across samples via principal component analysis. While little separation existed between the 5- and 10-dpf wt samples, the 5- and 10-dpf mzLrrk2 samples segregated, with 10-dpf mzLrrk2 clustering with controls (Figure 3c). In particular, mzLrrk2 microglia/leukocytes were on average larger and more ramified at 5 dpf, to then become smaller and less complex, comparable to the wt, at 10 dpf (Figure S4b–o). To test whether even mild morphological alterations correlated with impaired leukocyte function, 10-dpf larvae were treated with 12-*O*-tetradecanoylphorbol-13-acetate (TPA) to induce systemic acute inflammation [45] for 2 h prior to killing. Although treatment was not sufficient to elicit a substantial effect on the brain (not shown), significantly quenched leukocytosis was found in the tail (P=0.0368; Figure 3d, d'). In conclusion, our data suggest that zebrafish Lrrk2 plays a transient role in leukocyte biology, including a response to proinflammatory stimuli, and additionally hint that the recreation of pathological conditions in animal models, such as inflammation, may be an essential expedient for a thorough understanding of LRRK2 function.

Intact CA system but perturbed amine catabolism in older fish

Because catecholaminergic (CA) neurons are the most clinically relevant target of PD, special attention was paid to the CA system. CA cell populations along the rostro-caudal axis

from the olfactory bulb to the *locus cœruleus* were visualized via tyrosine hydroxylase (TH) immunohistochemistry and denominated after the nomenclature introduced previously [46] (Figure 4a). Zebrafish possess two paralogous *th* genes: *th1* and *th2* [47]. Because commercially available anti-TH antibodies only recognize TH1, but not TH2 protein [48], we analyzed the zebrafish CA system by double staining with an anti-TH1 antibody and a recently characterized pan-TH antibody to also identify TH2+ cells by exclusion (Figure 4a'). Additionally, the levels of biogenic amines and their catabolites (Figure 4b) were measured via electrochemical detection coupled with high performance liquid chromatography. We observed that no TH+ cell population was missing or overtly altered in mzLrrk2 fish. However, at 5 dpf, mzLrrk2 brains displayed lower numbers of TH+ cells in discrete populations: olfactory bulb (pop. 1, P=0.0313); telencephalic complex (pop. 2, P=0.0322); diencephalic complex (pop. 5, 6, 11, P=0.0042); and paraventricular organ, *partes intermedia* and *posterior* (pop. 9, 10 P=0.0042; Figure 4c, c'). The net effect was a 20% reduction of the overall number of TH+ cells (not shown). Because mzLrrk2 brains showed a higher cell death rate at 5 dpf (Figure 2a, a'), TUNEL assay was combined with TH immunohistochemistry to investigate whether CA neurons were selectively affected. However, virtually no colocalization was found (not shown). Consistently, the amine catabolism appeared normal (Figure 4d). At 10 dpf, only the hypothalamic complex (pop. 13, P=0.0403) and, mildly, the paraventricular organ, *pars posterior* (pop. 10b, P=0.0496) were affected; in contrast, an increase in the preoptic area, *pars posterior* (pop. 4, P=0.0138) was measured (Figure 4e, e'). In general, the overall number of TH+ cells did not differ from the controls (not shown). Intriguingly, although the dopamine catabolism was unaffected, a higher concentration of 5-hydroxyindoleacetic acid, a catabolite of serotonin, was measured (P=0.0190; Figure 4f). Because brain-specific effects could be masked in whole-larvae homogenates, the activity of monoamine oxidase (MAO), one of the two major catabolizing

enzymes, was histochemically visualized in 5- and 10-dpf brains (Figure 4g, h). However, no difference was observed between mzLrrk2 and controls.

In the adult brain, the CA system appeared structurally intact at 6 mo, with a modest increase in cell number in the telencephalic complex (pop. 2, P=0.0472; Figure 4i). Furthermore, TH1 protein levels at 11 mo were normal (Figure 4j). However, the amine catabolism in the brain was clearly perturbed in the older fish (Figure 4k). Specifically, a significant decrease of both dopamine (P=0.0216) and serotonin (P=0.0013) was found and, consistently, a significant increase in their catabolites 3,4-dihydroxyphenylacetic acid (P=0.0187), homovanillic acid (P=0.0001), and 5-hydroxyindoleacetic acid (P=0.0004), all products of MAO activity, was detected. However, MAO protein levels appeared unaltered, as determined on both gene expressional (Figure S5a) and biochemical level (Figure S5b). Nonetheless, the levels of the dopamine catabolite 3-methoxytyramine, product of catechol-*O*-methyltransferase activity, were not significantly different (P=0.1250; Figure 4k). Because monoamine oxidase and catechol-*O*-methyltransferase are the major enzymes responsible for catecholamine catabolism in the brain, we conclude that the neurochemical signatures observed were ascribable to MAO activity. In conclusion, although the cellular composition of the CA system appears morphologically unaltered, 11-mo mzLrrk2 fish show increased MAO-mediated amine degradation in the brain.

Decreased mitosis rate in the larval brain

Several lines of evidence point towards an involvement of mammalian LRRK2 in cell proliferation and differentiation [49]. Impaired neurogenesis and neurite outgrowth were reported in BAC human LRRK2 G2019S transgenic mice [50]. Knockout studies have, however, led to ambiguous findings: in mice, DCX+ neuroblasts in the dentate gyrus were increased in one study [51], but unaffected in another [29]. To assess cell proliferation in the zebrafish mzLrrk2 brain, we used phospho-histone H3 (pH3) as a marker for mitotic cells. At

5 dpf, mzLrrk2 brains displayed a significantly reduced number of mitotic cells in the anterior brain only (Figure 5a, a'; *P*=0.0052). However, the effect at 10 dpf accentuated, consisting in a 50% decrease in the anterior (*P*=0.0025) and middle brain portions (*P*=0.0062; Figure 5b, b'). The phenotype is clearly apparent only in maternal-zygotic individuals (Figure S6). Intriguingly, the number of cells in S phase of the cell cycle did not differ between mzLrrk2 and controls (anterior: *P*=0.6453; middle: *P*=0.1455; posterior: *P*=0.3613; Figure 5c), suggesting defects either in the progression or in the regulation of the cell cycle length. This is in line with previous evidence showing impaired cell cycle progression, survival and differentiation of human mesencephalic neural progenitor cells upon *LRRK2* knockdown [52]. Altered mitotic rate is not sufficient to cause overall altered brain size or morphology (not shown). Remarkably, the phenotype is merely emerging at 5 dpf and exacerbates by 10 dpf, i.e. during a time window when neural development slows down considerably, judging from the about nine-fold drop in the absolute number of total pH3+ cells in wt brains (5 dpf: 281.3±26.7; 10 dpf: 33.9±8.7).

To further validate our findings we carried out a complementation assay by combining the *lrrk2*^{tud113} allele with another *lrrk2* null allele to test recapitulation of the homozygous tud113 phenotype. We used a *N*-ethyl-*N*-nitrosourea-mutagenized *lrrk2* line (henceforth referred to as "tud112") generated in our lab [53] that carries a frameshift mutation (c.3972+2T>C) causing a premature stop within the LRR domain-coding region (p.(Ile1252AlafsTer9); Figure S7). Maternal-zygotic tud112 mutants demonstrated a similar decrease of mitosis in 8-dpf brains (Figure S7d). Upon crossing homozygous tud113 females with tud112 males, we confirmed the hypoproliferative phenotype also in 10 dpf- transheterozygotes (compared to wt, anterior: *P*=0.0002; middle: *P*=0.0007; Figure 5d).

Furthermore, we sought to 'rescue' Lrrk2 function by overexpressing a Lrrk2 protein fragment containing the catalytic core in mzLrrk2 mutants. To this aim, we generated a Tol2

transgenic line expressing a *lrrk2* rescue construct (c.3009_7130) along with an mCherry reporter under the heat-inducible *hsp70l* promoter (*Tg(hsp70l:mCherry-T2A-lrrk2(c.3009_7130)-Myc)*^{tud114}, henceforth referred to as "rescue"; Figure S8). The rescue line was combined with the tud113 line to determine if the maternal-zygotic phenotype can be rescued. Reconstituted fish were heat-shocked daily for 4 h from 1 to 10 dpf and analyzed for mitosis in the brain. Compared to wt controls, the overall number of pH3+ cells in the mzLrrk2+rescue recovered (P=0.1051), as opposed to mzLrrk2 controls (P=0.0034; Figure 5e, e'). This finding indicates that overexpression of a functional Lrrk2 protein fragment can rescue the mzLrrk2 phenotype. Altogether, our data reveal an implication of Lrrk2 in the control of cell proliferation in the developing brain.

Impaired neuronal regeneration in the adult telencephalon

Zebrafish have a remarkable capacity to regenerate lost or damaged tissues, including the telencephalon [54] and cerebellum [55]. Since regeneration recapitulates several aspects of embryonic development, we wondered whether loss of *lrrk2*, responsible for decreased cell proliferation in the larval brain, also affects reactive neurogenesis and regeneration in the adult brain. In unlesioned 6-mo old mzLrrk2 brains, we observed that proliferating cells, stained for the proliferation marker PCNA, are mildly reduced in the dorsal telencephalic niche, and significantly so in the dorso-posterior (Dp) area (P=0.0272; Figure S9). To address reactive proliferation and neurogenesis, 6-mo fish were injured using a stab lesion paradigm as previously described [54] (Figure 6a) and analyzed using a BrdU pulse-chase assay. Reactive proliferation at 3 days post-lesion (dpl) did not differ between mzLrrk2 and controls (Figure 6b). However, mzLrrk2 brains displayed on average 30% less HuC/D+/BrdU+ neurons at 21 dpl (P=0.0262; Figure 6c, c'). In contrast, neurogenesis in the unlesioned hemisphere was normal (P=0.284). Taken together, our results suggest a role for Lrrk2 in neuronal regeneration of the lesioned adult telencephalon.

Association between loss of *lrrk2* and hypokinesia in larvae

PD patients are characterized by a motor syndrome comprising resting tremor, rigidity, postural instability, and bradykinesia, or slowness of movement. To investigate motor ability after loss of *lrrk2*, spontaneous swimming activity of 5- and 10-dpf larvae and 6-mo adult fish was automatically recorded and analyzed. For each recording, a total of nine motor parameters were considered. The statistics for the individual parameters are reported in Figure S10. Because a complex set of changes may go unnoticed when considered in isolation, logistic regression was used to study the dependence of the genotype, a categorical variable with only two possible outcomes ("mzLrrk2" or "wt"), from a combination of the motor parameters. This is the same as using overall swimming performance as indicator of loss of *lrrk2*. The results are summarized in Table 2; each model's goodness of fit is provided in Figure S11.

Table 2. Multiple logistic regression analysis of the association of the swimming performance with the loss of *lrrk2*.

time point	independent variable	estimate (β)	OR (e^{β})	95% CI	*P*
5 dpf	inactive phase distance	–0.841	0.432	0.258–0.721	0.0014
	normal phase entry count	0.216	1.242	1.071–1.439	0.0041
	normal phase duration	–0.050	0.951	0.916–0.988	0.0091
	bursting phase duration	–0.269	0.764	0.628–0.929	0.0071
10 dpf	inactive phase entry count	–0.071	0.932	0.873–0.994	0.0316
	inactive phase duration	–0.033	0.968	0.948–0.988	0.0018
	inactive phase distance	0.521	1.684	1.149–2.468	0.0076
	normal phase duration	0.064	1.066	1.014–1.121	0.0126
	normal phase distance	–0.151	0.860	0.792–0.933	0.0003
	bursting phase duration	–0.166	0.847	0.735–1.976	0.0219

	bursting phase distance	0.177	1.194	1.079–1.321	0.0006
6 mo	normal phase distance	0.008	1.008	1.004–1.011	<0.0001
	bursting phase distance	0.003	1.003	1.002–1.004	<0.0001

The original motor variables (inactive/normal/bursting phase entry count/duration/distance for 5- and 10-dpf larvae; normal/bursting phase entry count/duration/distance for 6-mo adults) were subjected to backward stepwise elimination to identify the best fitting model at each time point. The selected variables and relative statistics are shown. For each variable, the odds ratio (OR) represents the change in the relative probability (p) of a recorded animal to be mzLrrk2 (p=1) over wt (p=0) for an x-unit change, the other variables held constant. Unit changes of x=10 for phase entry count and phase distance, x=1 for all other variables were deemed opportune. The estimated 95% confidence interval for each OR is reported. The intercept, i.e. the estimated OR when all covariates equal 0, is omitted.

At 5 dpf, the estimated odds ratios revealed that larvae were more likely to be mzLrrk2 if swimming more frequently at the normal speed range (normal phase entry count, OR=1.242) while spending less time in bursting swim mode (bursting phase duration, OR=0.764). At 10 dpf, mzLrrk2 larvae tended to alternate inactive to bursting phases (inactive phase distance, OR=1.684; bursting phase distance, OR=1.194), rather than swimming at the normal speed range (normal phase distance, OR=0.860), with lower cumulative bursting phase duration (OR=0.847). This "stop-and-go" swimming pattern might reflect an impaired ability to initiate or sustain movements, similar to bradykinesia in PD patients. However, at 6 mo, although the distance swum in either normal or bursting mode was a very strong predictor (P<0.0001 for both), the estimated odds ratios were very close to 1 (OR=1.008 and OR=1.003, respectively), indicating that the difference between adult mzLrrk2 fish and controls was very subtle.

Several non-motor symptoms often precede motor disease and aggravate disability in later stages of PD pathology. Anxiety and olfactory dysfunction are amongst the most prevalent in PD patients both after and prior to diagnosis [56]. Therefore, anxiety levels and response to

olfactory stimuli were analyzed in fish. To test anxiety levels, two paradigms were used: (i) wall-hugging behavior, or thigmotaxis, for both larvae and adults (Figure S12a–d), and (ii) dark-to-light preference, or scototaxis, for adults only (Figure S12e). To evaluate the overall olfactory function in adult fish, the response to an amino acid mixture odorant stimulus was measured (Figure S12f). None of the assays revealed any significant difference between mzLrrk2 fish and controls.

Discussion

Here we present the characterization of the brain phenotype of a complete zebrafish *lrrk2* knockout model (Figure 7). The homology between human LRRK2 and zebrafish Lrrk2 proteins (Figure 1a), the temporal and regional dynamics, and entity of *lrrk2* gene expression in the zebrafish brain from early embryo to adult (Figure S1, 2) make the zebrafish a suitable tool to study LRRK2 biology. The complete deletion of the entire *lrrk2* locus (Figure 1b) furthermore provides a genetically unambiguous tool to study LRRK2 deficiency in a vertebrate *in vivo*. The importance of this feat is twofold. First, because human LRRK2 variants are often considered to be gain-of-functions, great effort is being invested in the generation and evaluation of LRRK2 inhibitors [57]. However, pathogenicity of *Lrrk2* knockout in peripheral organs in rodents raise the possibility of alternative or additional loss-of-function contributions to disease pathology, as exemplified also by our examination of the *Lrrk2*-null phenotypes. In addition, a *lrrk2*-null zebrafish model is potentially applicable for high-throughput drug screening. In the context of PD modeling, alternatives to the gain-of-function hypothesis have been suggested before. Although human *LRRK2* nonsense mutations have been reported, though never associated with disease [38, 58], there is evidence supporting hypomorphic [25], dominant-negative [21, 23], and even protective [18, 59] effects of established PD-associated LRRK2 mutations. In fact, it has been hypothesized

that both “too much” or “too little” LRRK2 might detrimentally converge on synaptic function [60]. Being a completely amorphic model, the mzLrrk2 zebrafish model reported here represents a genetically unambiguous situation that provides novel opportunities for current and future investigations on LRRK2 loss-of-function.

In contrast with published MO-induced phenotypes [32, 34], we show that zebrafish *lrrk2* is a resilient locus (Figure 2–4). However, in contrast with previous Lrrk2 knockout studies in mice [29], we show that loss of *lrrk2* does have specific effects on the brain. In particular, mzLrrk2 larvae initially display reduced CA neurons and a combination of distinct motor signatures resembling hypokinesia, that however resolve spontaneously during further development. A possible reason for the lack of an overt PD-like phenotype in mzLrrk2 fish may be the lack of a zebrafish α-synuclein ortholog. Although α-synucleinopathy is not pathognomonic of PD, not even in *LRRK2* mutation carriers, progression of Lewy body pathology correlates with non-motor symptoms [3], including psychiatric disturbances and olfactory dysfunctions [61]. On these grounds, the normal anxiety levels and olfactory responsiveness in mzLrrk2 zebrafish that we observed seem reasonable (Figure S12). Yet, no PD-like brain pathology manifests in either transgenic [7-12] or knockout [29] *LRRK2* mouse models, where α-synuclein is present.

Strikingly, we observe perturbed amine catabolism, most prominently increased dopamine degradation, in 11-mo mzLrrk2 fish (Figure 4k). This result is particularly meaningful considering that brain dopamine and/or catabolite levels are normal in mice lacking endogenous [28, 29] or overexpressing human wild-type LRRK2 [11], but are reduced in mice expressing pathogenic LRRK2 variants, although the effect may be regional [10, 11] or transgene-dependent [11]. The neurochemical signatures in these mouse models have been difficult to interpret, because they are not clearly linked to problems in either dopamine synthesis [10] or turnover [10, 11]. In contrast, we specifically find enhanced monoamine

oxidase (MAO)-dependent amine degradation in mzLrrk2 fish. How this effect relates to loss of *lrrk2* is currently unclear, and hence it might be indirect. Previous observations have shown that both expression of the pathogenic LRRK2 R1441C variant [12] and *LRRK2* knockdown [62] impair synaptic transmission. If this is the case also for mzLrrk2 fish, increased MAO activity may be a protective mechanism against dopamine accumulation either at the presynaptic terminal, due to impaired neurotransmitter release, or at the synaptic cleft, due to impaired reuptake, as excess dopamine represents an oxidative threat due to radical formation [63]. However, while removing excess dopamine, MAO also generates toxic hydrogen peroxide [63], being potentially deleterious in the long term. Given the clinical relevance of MAO inhibitors as a treatment for PD [64], our findings highlight the importance to clarify the role of MAO given a predisposing genetic background.

An interesting question is whether mzLrrk2 fish may be protected, to some extent, from neurodegeneration by their potential to regenerate the brain after lesion [54, 55]. We provide compelling evidence that loss of *lrrk2* reduces the mitosis rate in the brain. The phenotype is specific to maternal-zygotic animals. Accordingly, *ad hoc* formation of cells to replace lost neurons is unlikely. However, this does not rule out that pro-regenerative cues may be present. Conceivably, the suppression of pro-regenerative mechanisms might aggravate the phenotype. One such mechanism may be protective autoimmunity [65]. Treatment with dexamethasone, a steroid anti-inflammatory drug, has been shown to dampen the regenerative ability of the zebrafish central nervous system [66, 67]. We verified that chronic exposure to dexamethasone has no influence on cell proliferation in 10-dpf mzLrrk2 brains (Figure S13). Therefore, if a regenerative response were underway, this would be independent of neuroinflammation. Other forms of plasticity might however come into play, including transdifferentiation [68]. Consequently, longitudinal studies will be needed to search for cell loss in aging fish.

Finally, we suggest that perturbing assays, such as the brain lesion we employed here, may reveal aspects of Lrrk2 pathobiology that are otherwise unnoticeable in unchallenged mzLrrk2 fish. In particular, we exploited the zebrafish as a regenerating organism and tested the brain reparative potential upon stabbing the adult telencephalon [54], and indeed, we observe impaired neuronal regeneration (Figure 6c–c''). We cannot rule out whether this conditional phenotype is an indirect consequence of the hypoproliferative phenotype we observe in the larval brain. Alternatively, the role of Lrrk2 in the control of cell proliferation may be more general during development, and more specialized later on in adult brains. Such a changing role could be reflected by *lrrk2* expression in the brain, which switches from being ubiquitous during development (Figure S1) to being more confined to specific areas in the adult brain, notably including the telencephalic neurogenic niche (Figure S2b–d). In either case, priming or supporting mechanisms might be required for Lrrk2 to partake in neuronal regeneration. Neuroinflammation appears as a promising candidate [44]. Of note, cultured rat microglia exhibit increased *LRRK2* expression upon acute inflammation and impaired inflammatory response upon *LRRK2* knockdown [69]. Furthermore, microglia in BAC human LRRK2 G2019S transgenic mice subjected to stab-wound or laser-injury display impaired ability to isolate the lesion site [70]. The zebrafish Lrrk2 may have a similar pro-inflammatory role, as suggested by our finding of reduced leukocytosis in larvae after TPA-induced systemic acute inflammation (Figure 3d, d'). Because acute inflammation is required for neuronal regeneration [66], a plausible scenario would then be that impaired production of neural precursor cells combined with defective microglia in mzLrrk2 fish impede brain repair. Transferred to humans, impaired LRRK2 function may lead to neurodegeneration through the accumulation of unresolved damages such as the ones following traumatic brain injury. Albeit recognized alone as a risk factor for PD [71], traumatic brain injuries are yet to

be examined in conjunction with known genetic factors, including *LRRK2* mutations. Targeted analyses on animal models and epidemiological studies are therefore warranted.

To summarize, our results show that loss of *lrrk2* can compromise specific vertebrate brain functions, including MAO-dependent amine catabolism and regenerative capacity upon lesion. We believe that similar defects in humans might play a contributing role in the prodromal stages of PD and are worth investigating further. To this aim, our zebrafish *lrrk2* knockout model offers a unique possibility to study *in vivo* the consequences of LRRK2 loss of function in a regenerating vertebrate system and, coupled with the well-established high-throughput screening amenability of zebrafish, provides a means for identifying targets of interest in a fish-to-mammal translational perspective.

Methods

Ethics statement

All animal experiments were conducted according to the guidelines and under supervision of the Regierungspräsidium Dresden (permits AZ: 24D-9168.11-1/2008-2; AZ: 24D-9168.11-1/2008-3; AZ: 24-9168.11-1/2013-5; AZ: 24-9168.11-1/2013-14; DD24-5131/346/11; DD24-5131/346/12). All efforts were made to minimize animal suffering and the number of animals used.

Sequence alignment analyses

Sequences were retrieved from the latest assemblies of the human and zebrafish genomes (GRCh38p.7 and GRCz10, respectively). Alignment analyses were performed using Clustal Omega [72] and BLAST [73].

Cas9 and gRNA construction

Cas9 mRNA and gRNAs were synthesized as previously described [74]. Briefly, *Cas9* mRNA was synthesized by *in vitro* transcription using T3 mMESSAGE mMACHINE kit (Ambion). gRNAs were generated and purified using the MEGAshortscript T7 and *mir*Vana miRNA isolation kits (Ambion), respectively. Sequences of the genomic target sites and oligonucleotides for making gRNAs are listed in Table 3.

Table 3. gRNA target sites for *lrrk2* locus deletion.

Target site	oligonucleotide for annealing	
GGGATGTTAATGTGTCAACA	TA**GGGATGTTAATGTGTCA**	AAAC**TGTTGACACATTAAC**
TGG	**ACA**	**ATC**
*CCG***CCATCGACAACTCCCTG**	TA**GGACAGGGAGTTGTCGA**	AAAC**CCATCGACAACTCCC**
TCA	**TGG**	**TGT**

Sequences are oriented 5' to 3'. Target site PAMs are italicised and underscored. Sequences present in the gRNAs are bold.

Plasmid construction

A *lrrk2* cDNA fragment (c.3009_7130 according to the Human Genome Variation Society guidelines [39]) flanked by BamHI (5') and ClaI (3') restriction sites was cloned into a *pCS2+MT* vector [75]. The *lrrk2* rescue fragment including the 5x*Myc* repeat, the TAG stop codon, the poly(A) signal, and flanked by NheI (5') and AscI (3') restriction sites was cloned into the vector *pTol(hsp70l:mCherry-T2A-CreER*^{T2}) [76] to result in the simultaneous expression of the corresponding Lrrk2 protein fragment and the mCherry reporter under the control of the heat-inducible *hsp70l* promoter. Primers used for cloning are reported in Table 4.

Table 4. Primers used.

Primer sequence	target locus	application
F: CTCTGGATCCGCCACCATGCAGATTGCAAACCTTCATCGGCTCG R: CTCTATCGATTCTTGTCCCAGACCTCAACAGTGTG	*lrrk2*	cloning into pCS2+MT vector
F: ATCCGCTAGCATGCAGATTGCAAACCTTCATCGGCTC R: AAGGGGCGCGCCGCTGGGTACCGGGCCCAATGCATTGGCG	*lrrk2*	cloning into pTol vector
F: TACAAGTGGGCCCGACTGGAGAAAC R: ATCCAGAGGCAGATCCCACAGATGC	*lrrk2*	genotyping for the hu3557 allele
F1: TGCGAGCGCTGTCTGCTGTTAC R1: TGTCTTTGCTCCTGACGGGCCA F2: TACACAGGCGCCAACATGACCG R2: AGCTACACGCTGGACTTGGGGT	*lrrk2*	genotyping for the del allele
F1: TCTGCTGAACTGGATGTTGGC R1: TAATCAAACCCCACGGCACC	*lrrk1*	ISH probe 1
F2: GGAGCCCAGTGAAAAAAACCC R2: GAACGGTGATGCGAGACGAC	*lrrk1*	ISH probe 2
F3: TCCTGTGTTTGGCAGCTCAGAATG R1	*lrrk1*	ISH probe 3
F: CGTGAAGGTTTTCCAAGCTGCT R: CTAACTCCCACAATCCCCTTCTTC	*lrrk2*	ISH probe 1
F: GGTCTTTTGGCTGCTGGTTGTAAC R: CGGTTTGGGTTTGGTGTCAATG	*lrrk2*	ISH probe 2
F: CTTCAACATGGAGGACTGCG R: CGTGAGGGGAAGTCTGTCAT	*lrrk1*	RT-qPCR
F: GGACCAGTCTAGACCGATGG	*lrrk2*	RT-qPCR

R: CAAAATGTGTCCCGCTCTCG		
F1: **TGTTTCCCAGTATTGGGTTG**	*lrrk2*	TILLING screening[a]
R1: **GCAGATGGCGCTCTAGG**		
F2: TGTAAAACGACGGCCAGT**GCTGGAATAGTTGGTGGTTC**		
R2: AGGAAACAGCTATGACCAT**TAACCTGTCCGCAATAACAC**		
F: TATGCTCGTGTCCTGGGATC	*mao*	RT-qPCR
R: CAAGACCCTGCCAAACTGTG		
F: CCTTCCTGGGTATGGAATCT	*actb1*	RT-qPCR
R: GACAGCACTGTGTTGGCATA		
F: GTGCCCATCTACGAGGGTTA	*actb2*	RT-qPCR [66]
R: TCTCAGCTGTGGTGGTGAAG		

All primers target the indicated locus or flanking regions. Sequences are oriented 5' to 3'. Primers used for genotyping were used on genomic DNA template; else, cDNA. Abbreviations: F, forward primer; R, reverse primer.

[a]Sequences present in the *lrrk2* gene are bold.

TILLING and TALEN screening

Targeting induced local lesion in genomes (TILLING) mutagenesis screening was performed as previously described [53]. Outer (F1, R1) and inner (F2, R2) primers used are reported in Table 4. During the screening the allele *hu3557*, a splice mutation affecting the splice donor of *lrrk2* exon 27 (c.3972+2T>C) was recovered and designated as "tud112". We also generated an additional, early stop codon-carrying *lrrk2* allele (c.1980_1990del) using transcription activator-like effector nucleases (TALENs), denominated *tud115*, which however could give rise to a truncated Lrrk2 product from a downstream alternative translation initiation site, and was therefore not considered further.

Zebrafish husbandry and germ line transformation

Zebrafish were raised and maintained as previously described [77]. Zebrafish embryos were obtained by natural spawnings of adult fish and staged according to hours post fertilization (hpf) or standard criteria [78]. The wild-type line used was AB. For CRISPR/Cas9-mediated mutagenesis, 150 ng/μL dual NLS-tagged zebrafish codon-optimized *cas9* mRNA/50 ng/μL gRNAs/0.2% phenol red were co-injected into fertilized eggs, the embryos raised to adulthood, crossed to AB wild-type fish and the resulting F1 embryos screened by PCR. The identified mutation (c.–61_*42del; see Results section) was designated as "tud113". For germ line transformation, plasmid DNA (*pTol(hsp70l:mCherry-T2A-lrrk2(c.3009_7130)-Myc)*) and transposase mRNA were injected into fertilized eggs (F0), raised to adulthood and crossed to AB wild-type fish as previously described [79]. To identify transgenic carriers, undechorionated F1 embryos at 20 hpf were heat-shocked, examined under a fluorescent microscope after a 4 h waiting period and positive embryos were raised. The established line was designated as "tud114".

Genotyping

Genotyping was performed using genomic DNA from individual or pooled embryos/larvae or fin clips from larvae or adult fish. Primers used are listed in Table 4. For genotyping for the *lrrk2*^{tud113} allele, see Results section. For genotyping for the *lrrk2*^{tud112} allele, see Figure S7.

Animal experiments

Fin clipping for genotyping purposes was performed on adult fish following anesthesia with 0.02% tricaine. Drug treatments are summarized in Table 5. Heat shocks were administered daily from 1 to 10 days post-fertilization (dpf). Treatment consisted in sudden exposure to 42 ºC E3 medium, followed by 4 h incubation at 37 ºC. Fish were sacrificed 4 h after the last heat shock. Stab lesions were performed on male adult fish as previously described [54].

Table 5. Summary of drug treatments.

Drug	dose and solvent	exposure
BrdU	for larvae: 10 μM, E3 medium	3 h
	for adults: 5 μM, fish water	24 h
Dexamethasone	10 μM from 25 mg/mL MetOH stock, autoclaved E3 medium	9 d[a]
	control: MetOH equivalent, autoclaved E3 medium	
TPA	10 ng/ml from 50 μg/mL DMSO stock, E3 medium;	2 h
	control: DMSO equivalent, E3 medium	

All drugs were purchased from Sigma. Abbreviations: BrdU, 5-bromo-2'-deoxyuridine; DMSO, dimethyl sulfoxide; MetOH, methanol; TPA, 12-*O*-tetradecanoylphorbol-13-acetate.

[a]From 1 to 10 dpf, solution changed daily.

Behavioral analyses

The ZebraBox and ZebraCube apparatus were used in combination with the Viewpoint Application Manager software. All recordings were performed on individually isolated animals between 2–6 pm. Larvae at 4 dpf were transferred into 24-well plates and therein grown until 10 dpf. Each well was internally lined with Parafilm to minimize reflection and filled with 750 μL E3 medium, changed daily. Animals whose tracking was lost by the software for over 20% of the total recording time were excluded from the analyses. To quantify spontaneous swimming and thigmotaxis, adult fish were lodged in opaque cylindrical boxes (ø=80 mm) filled with 100 mL fish facility water, else in opaque parallelepipedal boxes (l×w=190×80 mm) filled with 500 mL fish facility water. Each recording was preceded by 10 min acclimatization inside the apparatus. Spontaneous swimming was assessed for 10 min (integration period: 600 s) in the dark under infrared light. Appropriate speed thresholds were chosen based on developmental stage: 2–10 mm/s for larvae; 2–40 mm/s for adults. Based on the speed thresholds, three swimming phases were

defined: inactive phase, below the lower threshold; normal swimming phase, between the lower and upper threshold; bursting phase, above the upper threshold. For each swimming phase, three parameters were considered: entry count, duration (s), and distance swum (mm). Thigmotaxis was assessed using the same recordings of spontaneous swimming activity. To this aim, the recording arena was digitally subdivided into an outer and inner area (for larvae ø=15.6/10.6 mm; for adults ø=80/55 mm). Scototaxis was assessed for 10 min in half-black, half-white parallelepipedal boxes. Olfactory function was assessed by delivering a stimulus in either of the shorter sides of parallelepipedal boxes. The stimulus consisted in 0.6 mL of an amino acid mix (Ala, Cys, His, Lys, Met, Val, 0.1 mM each) delivered through a syringe pump (1.5 mL/min). Fish were starved for 24 h before the experiments. Fish behavior was recorded 5 min before and 5 min after stimulus delivery. For every 1 min of recording, a preference index was defined [80] as $\frac{ts-tc}{ts+tc}$, where ts is the time spent in the stimulus side, tc the time spent in the control side.

Tissue processing and histochemistry

Tissue processing is summarized in Table 6. Bleaching was performed using 3% hydrogen peroxide/0.1% Tween20/1% potassium hydroxide. Clearing [81] was carried out overnight at room temperature. The procedure caused slight swelling of tissue, more pronounced in younger samples. Immunohistochemistry (IHC) was performed as previously described on whole embryos/larvae [82], dissected larval brains [46], and cryosections [83]. Primary antibodies used are listed in Table 7. Secondary antibodies (1:500) were conjugated to Alexa Fluor 488, 555, 633, 700 (Invitrogen). For combined staining with one or more antibodies requiring antigen retrieval the following precautions were used: HuC/D IHC was performed first if combined with BrdU IHC, otherwise last; PCNA, TH(1) IHC were performed last. TUNEL assay on larval brains was carried out using the ApopTag Red or Fluorescein *In Situ* Apoptosis Detection Kits (Millipore) according to the manufacturer's instructions with the

following adjustments: tissue was washed 3×10 min with sodium citrate/Triton X-100 0.1% in PBS prior to acetic acid/ethanol post-fixation; incubation in the equilibration buffer was carried out for 1 h at room temperature. When combined with IHC, TUNEL assay was performed first. *In situ* hybridization (ISH) and probe generation were performed on embryos and at least three adult individuals [84]. All synthesized and individually tested probes (Table 4) showed a redundant pattern. Monoamine oxidase histochemistry (MAO HC) was carried out as previously described [46] with the following adjustments: staining was developed for 90 min; stained tissue was post-fixed in 4% paraformaldehyde.

Table 6. Summary of tissue processing.

Tissue	application	fixation	bleaching	clearing
embryos (24–48 hpf)	IHC, ISH	4% PFA	yes (from 32 hpf)	no
larvae (5, 10 dpf)	IHC (dissected brains, tails)	2% PFA/1% DMSO	yes	yes
	Mao HC (dissected brains)	4% EDAC/0.4% NHS/1% DMSO	no	no
adult heads (sections)	IHC, ISH	4% PFA	no	no

Abbreviations: EDAC, 1-ethyl-3-(3-dimethylaminopropyl)carbodiimide; NHS, *N*-hydroxysuccinimide; PFA, paraformaldehyde.

Table 7. Primary antibodies used.

antigen, host (company)	antigen retrieval	dilution
acetylated Tubulin, mouse IgG_{2b} (Sigma)	no	1:1,000
BrdU, rat (Serotec)	2 N hydrochloric acid for 20 min at 37°C, followed by 5 min was in 0.1% sodium tetraborate buffer, pH=8.5	1:500

Claudin k, rat[85]	no	1:1,000
DsRed, rabbit (Clontech)[a]	no	1:1,000
HuC/D, mouse IgG_{2b} (Molecular Probes)	Tris-HCl buffer, pH=8.0 for 5 min at 98°C	1:200
L-Plastin, rabbit[86][b]	no	1:5,000
MYC, mouse IgG_1 (Santa Cruz)	no	1:1,000
PCNA, mouse IgG_{2a} (Dako)	10 mM sodium citrate buffer, pH=6.0 for 15 min at 85°C	1:500
pH3, rabbit (Millipore)	no	1:200
TH(1), mouse IgG_1 (Immunostar)	for larval brains: no	1:1,000
	for adult brains: 10 mM sodium citrate buffer, pH=6.0 for 15 min at 85°C	1:1,000
TH(1/2), rabbit[48, 87]	no	1:1,000

Abbreviations: PCNA, proliferating cell nuclear antigen; TH(1), tyrosine hydroxylase (isoform 1); TH(1/2), tyrosine hydroxylase (isoforms 1 and 2).

[a]The antibody also recognizes mCherry.

[b]Homemade antibody, expression plasmid provided by M.J. Redd.

High performance liquid chromatography measurements

Tissue samples consisted each in 10-pooled whole larvae or single adult brain. Larvae were starved 24 h before tissue collection to minimize possible contamination from amines in the gastrointestinal tract. An equal number of male and female adult fish were sacrificed. Tissue homogenization and catabolite measurements via electrochemical detection coupled with high performance liquid chromatography (HPLC) were performed as previously described [46].

Immunoblotting

Protein pellets obtained from the tissue samples used in HPLC were homogenized by sonication at room temperature in 5% SDS in PBS, pH 7.4, to perform the BCA assay. The

solutions were then diluted with a loading buffer stock containing Tris-HCl, pH 6.8, β-mercaptoethanol, glycerol, and bromophenol blue (final concentration: 0.0625 M Tris-HCl, 5% β -mercaptoethanol, 10% glycerol, and 0.002% bromophenol blue). The samples were heated at 95°C for 5 min and loaded on a gel for SDS-PAGE (4% stacking gel, 9% separating gel). The loading volume was adjusted in order to load 20 μg total protein per well. PageRuler Prestained protein markers (Thermo Scientific) were used to control protein separation. The proteins were electrophoretically transferred to an Immobilon P PVDF membrane in an eBlot device (GenScript) according to the manufacturer's instructions and the membrane was processed for immunoblotting in an Odyssey CLx system (Li-Cor) according to the manufacturer's instructions. Mouse monoclonal anti-TH(1) antibody (Immunostar) diluted was used as the primary antibody (1:2,000), and a goat anti-mouse IRDye800 antibody (Li-Cor) was used as the secondary antibody (1:20,000). The fluorescent bands were quantitated by the ImageStudio software supplied with the Odyssey CLx system, and the membranes were stained with ProAct membrane stain (M282–1L, Amresco Inc.) as the loading control.

MAO activity assay

Peroxidase-linked colorimetric assay of MAO activity was performed as previously described [88].

RNA extraction and RT-qPCR

Total RNA was isolated from pooled embryos using TRIzol (Invitrogen). cDNA was generated using Superscript III First Strand Synthesis System (Invitrogen). Reverse transcriptase-quantitative PCR (RT-qPCR) was performed using the LightCycler 480 SYBR Green I Master mix and the LightCycler 480 Instrument (Roche). Target gene expression was normalized by *actb1* or *actb2* expression.

Image acquisition and processing

Confocal images were acquired with a Zeiss LSM 780 upright confocal microscope using C-Apochromat 10x/0.45 W and LD LCI Plan-Apochromat 25x/0.8 Imm Corr DIC M27 objectives for water immersion. Bright-field images were acquired with an Olympus DP71 or DP80 color cameras connected to an MVX10 microscope. All devices were provided by the BIOTEC/CRTD Light Microscopy Facility. Images were processed using Fiji [89]. Processing was applied equally across entire images and to controls. Cell quantification was carried out manually through whole stacks. To analyze microglia/leukocyte morphology and complexity, confocal stacks were background-subtracted using the sliding paraboloid method, despeckled, and thresholded using Li's method (Figure S4a–a'''). Obvious artifacts were manually removed from subsequent processing and analyses. The 3D ImageJ Suite plugin [90] was used to segment objects (minimum size threshold: 1,000; objects on borders excluded) and extract morphological data from 3D masks. The same 3D masks were subsequently skeletonized and subjected to 3D skeleton analysis using the AnalyzeSkeleton plugin on Fiji [91]. Loops were pruned using the shortest branch method. For each skeleton, the longest shortest path was also calculated. A ramification index was defined as $\frac{2b}{j+e}$, where b is the number of branches, j the number of junctions, e the number of end-points, as previously defined [91].

Statistical analyses

The data analysis for this paper was generated using: the Real Statistics Resource Pack software (Release for Mac 3.1.2, copyright 2013–2016) developed by C. Zaiontz (www.real-statistics.com); R [92]; and GraphPad Prism version 7.0b for Mac OS X. To compare means, requirements of normal distribution and homoscedasticity were checked using Shapiro-Wilk's test and the F-test, for two groups, or Levene's test, for more than two groups, respectively. To determine the statistical significance of group differences, *P* values were

calculated using: Student's *t*-test or ANOVA, for normally distributed and homoscedastic data; Student's t-test with Welch's correction, for normally distributed and heteroscedastic data; Mann-Whitney's *U*-test for non-normally distributed data. Multiple comparisons following ANOVA were performed using Dunn-Šidák's method. For multivariate logistic regression analyses, the best fitting models were automatically selected via backward stepwise elimination. The model performance was visualized and assessed using the methods previously described [93]. For each experiment, sample sizes are reported in the Figures. Plot features are described in the Figure legends. Within the Figures, significant comparisons are marked by asterisks: *, $P<0.05$; **, $P<0.01$; ***, $P<0.001$; ****, $P<0.0001$. *P* values rounded to three decimal places are reported in the Figure graphs for values comprised between 0.050 and 0.059; *P* values rounded to four decimal places are reported in the main text.

Acknowledgments

The authors express thanks to: our histology facility, light microscopy facility, and fish facility for excellent support; M. Reimer (CRTD) for providing the anti-Claudin k antibody; M.J. Redd (Department of Pathology, University of Utah, Salt Lake City, Utah, USA) for providing the anti-L-Plastin antibody; J. Guck (BIOTEC) for providing the syringe pump; J. Sterneckert, G. Kempermann, and W. Schlechte-Wełnicz (CRTD) for comments on the manuscript, and our funding agencies, as indicated, for support.

References

1. Guo L, Gandhi PN, Wang W, Petersen RB, Wilson-Delfosse AL, Chen SG. The Parkinson's disease-associated protein, leucine-rich repeat kinase 2 (LRRK2), is an authentic GTPase that stimulates kinase activity. Experimental cell research. 2007;313(16):3658-70. Epub 2007/08/21. doi: 10.1016/j.yexcr.2007.07.007. PubMed PMID: 17706965; PubMed Central PMCID: PMCPMC2083285.

2. Drolet RE, Sanders JM, Kern JT. Leucine-rich repeat kinase 2 (LRRK2) cellular biology: a review of recent advances in identifying physiological substrates and cellular functions. Journal of neurogenetics. 2011;25(4):140-51. Epub 2011/11/15. doi: 10.3109/01677063.2011.627072. PubMed PMID: 22077787.

3. Kalia LV, Lang AE, Hazrati L, et al. Clinical correlations with lewy body pathology in lrrk2-related parkinson disease. JAMA neurology. 2015;72(1):100-5. doi: 10.1001/jamaneurol.2014.2704.

4. Spillantini MG, Goedert M. The alpha-synucleinopathies: Parkinson's disease, dementia with Lewy bodies, and multiple system atrophy. Annals of the New York Academy of Sciences. 2000;920:16-27. Epub 2001/02/24. PubMed PMID: 11193145.

5. Gloeckner CJ, Kinkl N, Schumacher A, Braun RJ, O'Neill E, Meitinger T, et al. The Parkinson disease causing LRRK2 mutation I2020T is associated with increased kinase activity. Hum Mol Genet. 2006;15(2):223-32. Epub 2005/12/03. doi: 10.1093/hmg/ddi439. PubMed PMID: 16321986.

6. West AB, Moore DJ, Biskup S, Bugayenko A, Smith WW, Ross CA, et al. Parkinson's disease-associated mutations in leucine-rich repeat kinase 2 augment kinase activity. Proceedings of the National Academy of Sciences of the United States of America. 2005;102(46):16842-7. doi: 10.1073/pnas.0507360102. PubMed PMID: PMC1283829.

7. Lin X, Parisiadou L, Gu X-L, Wang L, Shim H, Sun L, et al. Leucine-Rich Repeat Kinase 2 Regulates the Progression of Neuropathology Induced by Parkinson's Disease-related Mutant α-synuclein. Neuron. 2009;64(6):807-27. doi: 10.1016/j.neuron.2009.11.006. PubMed PMID: PMC2807409.

8. Garcia-Miralles M, Coomaraswamy J, Häbig K, Herzig MC, Funk N, Gillardon F, et al. No Dopamine Cell Loss or Changes in Cytoskeleton Function in Transgenic Mice Expressing Physiological Levels of Wild Type or G2019S Mutant LRRK2 and in Human Fibroblasts. PLoS ONE. 2015;10(4):e0118947. doi: 10.1371/journal.pone.0118947. PubMed PMID: PMC4382199.

9. Li Y, Liu W, Oo TF, Wang L, Tang Y, Jackson-Lewis V, et al. Mutant LRRK2(R1441G) BAC transgenic mice recapitulate cardinal features of Parkinson's disease. Nature neuroscience. 2009;12(7):826-8. doi: 10.1038/nn.2349. PubMed PMID: PMC2845930.

10. Maekawa T, Mori S, Sasaki Y, Miyajima T, Azuma S, Ohta E, et al. The I2020T Leucine-rich repeat kinase 2 transgenic mouse exhibits impaired locomotive ability accompanied by dopaminergic neuron abnormalities. Mol Neurodegener. 2012;7:15. Epub 2012/04/27. doi: 10.1186/1750-1326-7-15. PubMed PMID: 22534020; PubMed Central PMCID: PMCPMC3467184.

11. Ramonet D, Daher JPL, Lin BM, Stafa K, Kim J, Banerjee R, et al. Dopaminergic Neuronal Loss, Reduced Neurite Complexity and Autophagic Abnormalities in Transgenic Mice Expressing G2019S Mutant LRRK2. PLOS ONE. 2011;6(4):e18568. doi: 10.1371/journal.pone.0018568.

12. Tong Y, Pisani A, Martella G, Karouani M, Yamaguchi H, Pothos EN, et al. R1441C mutation in LRRK2 impairs dopaminergic neurotransmission in mice. Proc Natl Acad Sci U S A. 2009;106(34):14622-7. Epub 2009/08/12. doi: 10.1073/pnas.0906334106. PubMed PMID: 19667187; PubMed Central PMCID: PMCPMC2732807.

13. Yue M, Hinkle K, Davies P, Trushina E, Fiesel F, Christenson T, et al. Progressive dopaminergic alterations and mitochondrial abnormalities in LRRK2 G2019S knock in mice. Neurobiology of disease. 2015;78:172-95. doi: 10.1016/j.nbd.2015.02.031. PubMed PMID: PMC4526103.

14. Dusonchet J, Kochubey O, Stafa K, Young SM, Jr., Zufferey R, Moore DJ, et al. A rat model of progressive nigral neurodegeneration induced by the Parkinson's disease-associated G2019S mutation in LRRK2. J Neurosci. 2011;31(3):907-12. Epub 2011/01/21. doi: 10.1523/jneurosci.5092-10.2011. PubMed PMID: 21248115.

15. Tsika E, Nguyen AP, Dusonchet J, Colin P, Schneider BL, Moore DJ. Adenoviral-mediated expression of G2019S LRRK2 induces striatal pathology in a kinase-dependent manner in a rat model of Parkinson's disease. Neurobiology of disease. 2015;77:49-61. Epub 2015/03/04. doi: 10.1016/j.nbd.2015.02.019. PubMed PMID: 25731749.

16. Chen CY, Weng YH, Chien KY, Lin KJ, Yeh TH, Cheng YP, et al. (G2019S) LRRK2 activates MKK4-JNK pathway and causes degeneration of SN dopaminergic neurons in a transgenic mouse model of PD. Cell Death and Differentiation. 2012;19(10):1623-33. doi: 10.1038/cdd.2012.42. PubMed PMID: PMC3438494.

17. Lee BD, Shin J-H, VanKampen J, Petrucelli L, West AB, Ko HS, et al. Inhibitors of Leucine Rich Repeat Kinase 2 (LRRK2) Protect Against LRRK2-Models of Parkinson's

Disease. Nature medicine. 2010;16(9):998-1000. doi: 10.1038/nm.2199. PubMed PMID: PMC2935926.

18. Longo F, Russo I, Shimshek DR, Greggio E, Morari M. Genetic and pharmacological evidence that G2019S LRRK2 confers a hyperkinetic phenotype, resistant to motor decline associated with aging. Neurobiology of disease. 2014;71:62-73. doi: 10.1016/j.nbd.2014.07.013. PubMed PMID: PMC4194318.

19. Funayama M, Li Y, Tomiyama H, Yoshino H, Imamichi Y, Yamamoto M, et al. Leucine-rich repeat kinase 2 G2385R variant is a risk factor for Parkinson disease in Asian population. Neuroreport. 2007;18(3):273-5. Epub 2007/02/23. doi: 10.1097/WNR.0b013e32801254b6. PubMed PMID: 17314670.

20. Di Fonzo A, Wu-Chou Y-H, Lu C-S, van Doeselaar M, Simons EJ, Rohé CF, et al. A common missense variant in the LRRK2 gene, Gly2385Arg, associated with Parkinson's disease risk in Taiwan. Neurogenetics. 2006;7(3):133-8. doi: 10.1007/s10048-006-0041-5.

21. Rudenko IN, Kaganovich A, Hauser DN, Beylina A, Chia R, Ding J, et al. The G2385R Variant of Leucine-Rich Repeat Kinase 2 Associated with Parkinson's Disease is a Partial Loss of Function Mutation. The Biochemical journal. 2012;446(1):99-111. doi: 10.1042/BJ20120637. PubMed PMID: PMC4667980.

22. Ho DH, Jang J, Joe E-h, Son I, Seo H, Seol W. G2385R and I2020T Mutations Increase LRRK2 GTPase Activity. BioMed Research International. 2016;2016:7917128. doi: 10.1155/2016/7917128. PubMed PMID: PMC4897664.

23. Ohta E, Kawakami F, Kubo M, Obata F. Dominant-negative effects of LRRK2 heterodimers: a possible mechanism of neurodegeneration in Parkinson's disease caused by LRRK2 I2020T mutation. Biochemical and biophysical research communications. 2013;430(2):560-6. Epub 2012/12/12. doi: 10.1016/j.bbrc.2012.11.113. PubMed PMID: 23220480.

24. Jaleel M, Nichols RJ, Deak M, Campbell DG, Gillardon F, Knebel A, et al. LRRK2 phosphorylates moesin at threonine-558: characterization of how Parkinson's disease mutants affect kinase activity. Biochem J. 2007;405(2):307-17. Epub 2007/04/24. doi: 10.1042/bj20070209. PubMed PMID: 17447891; PubMed Central PMCID: PMCPMC1904520.

25. Nichols R J, Dzamko N, Morrice Nicholas A, Campbell David G, Deak M, Ordureau A, et al. 14-3-3 binding to LRRK2 is disrupted by multiple Parkinson's disease-associated mutations and regulates cytoplasmic localization. Biochemical Journal. 2010;430(Pt 3):393-404. doi: 10.1042/BJ20100483. PubMed PMID: PMC2932554.

26. Baptista MA, Dave KD, Frasier MA, Sherer TB, Greeley M, Beck MJ, et al. Loss of leucine-rich repeat kinase 2 (LRRK2) in rats leads to progressive abnormal phenotypes in peripheral organs. PLoS One. 2013;8(11):e80705. Epub 2013/11/19. doi: 10.1371/journal.pone.0080705. PubMed PMID: 24244710; PubMed Central PMCID: PMCPMC3828242.

27. Herzig MC, Kolly C, Persohn E, Theil D, Schweizer T, Hafner T, et al. LRRK2 protein levels are determined by kinase function and are crucial for kidney and lung homeostasis in mice. Human Molecular Genetics. 2011;20(21):4209-23. doi: 10.1093/hmg/ddr348. PubMed PMID: PMC3188995.

28. Tong Y, Yamaguchi H, Giaime E, Boyle S, Kopan R, Kelleher RJ, et al. Loss of leucine-rich repeat kinase 2 causes impairment of protein degradation pathways, accumulation of α-synuclein, and apoptotic cell death in aged mice. Proceedings of the National Academy of Sciences of the United States of America. 2010;107(21):9879-84. doi: 10.1073/pnas.1004676107. PubMed PMID: PMC2906862.

29. Hinkle KM, Yue M, Behrouz B, Dachsel JC, Lincoln SJ, Bowles EE, et al. LRRK2 knockout mice have an intact dopaminergic system but display alterations in exploratory and motor co-ordination behaviors. Mol Neurodegener. 2012;7:25. Epub 2012/06/01. doi: 10.1186/1750-1326-7-25. PubMed PMID: 22647713; PubMed Central PMCID: PMCPMC3441373.

30. Melrose HL, Dächsel JC, Behrouz B, Lincoln SJ, Yue M, Hinkle KM, et al. Impaired dopaminergic neurotransmission and microtubule-associated protein tau alterations in human LRRK2 transgenic mice. Neurobiology of disease. 2010;40(3):503-17. doi: http://dx.doi.org/10.1016/j.nbd.2010.07.010.

31. Kizil C, Kaslin J, Kroehne V, Brand M. Adult neurogenesis and brain regeneration in zebrafish. Developmental neurobiology. 2012;72(3):429-61. Epub 2011/05/20. doi: 10.1002/dneu.20918. PubMed PMID: 21595047.

32. Sheng D, Qu D, Kwok KH, Ng SS, Lim AY, Aw SS, et al. Deletion of the WD40 domain of LRRK2 in Zebrafish causes Parkinsonism-like loss of neurons and locomotive defect. PLoS Genet. 2010;6(4):e1000914. doi: 10.1371/journal.pgen.1000914. PubMed PMID: 20421934; PubMed Central PMCID: PMCPMC2858694.

33. Ren G, Xin S, Li S, Zhong H, Lin S. Disruption of LRRK2 does not cause specific loss of dopaminergic neurons in zebrafish. PLoS One. 2011;6(6):e20630. doi: 10.1371/journal.pone.0020630. PubMed PMID: 21698186; PubMed Central PMCID: PMCPMC3116841.

34. Prabhudesai S, Bensabeur FZ, Abdullah R, Basak I, Baez S, Alves G, et al. LRRK2 knockdown in zebrafish causes developmental defects, neuronal loss, and synuclein aggregation. J Neurosci Res. 2016;94(8):717-35. doi: 10.1002/jnr.23754. PubMed PMID: 27265751.

35. Kok Fatma O, Shin M, Ni C-W, Gupta A, Grosse Ann S, van Impel A, et al. Reverse Genetic Screening Reveals Poor Correlation between Morpholino-Induced and Mutant Phenotypes in Zebrafish. Developmental Cell. 2015;32(1):97-108. doi: http://dx.doi.org/10.1016/j.devcel.2014.11.018.

36. Rossi A, Kontarakis Z, Gerri C, Nolte H, Holper S, Kruger M, et al. Genetic compensation induced by deleterious mutations but not gene knockdowns. Nature. 2015;524(7564):230-3. doi: 10.1038/nature14580

http://www.nature.com/nature/journal/v524/n7564/abs/nature14580.html - supplementary-information.

37. Cruts M, Theuns J, Van Broeckhoven C. Locus-specific mutation databases for neurodegenerative brain diseases. Hum Mutat. 2012;33(9):1340-4. Epub 2012/05/15. doi: 10.1002/humu.22117. PubMed PMID: 22581678; PubMed Central PMCID: PMCPMC3465795.

38. Nuytemans K, Theuns J, Cruts M, Van Broeckhoven C. Genetic etiology of Parkinson disease associated with mutations in the SNCA, PARK2, PINK1, PARK7, and LRRK2 genes: a mutation update. Hum Mutat. 2010;31(7):763-80. Epub 2010/05/28. doi: 10.1002/humu.21277. PubMed PMID: 20506312; PubMed Central PMCID: PMCPMC3056147.

39. den Dunnen JT, Dalgleish R, Maglott DR, Hart RK, Greenblatt MS, McGowan-Jordan J, et al. HGVS Recommendations for the Description of Sequence Variants: 2016 Update. Human Mutation. 2016;37(6):564-9. doi: 10.1002/humu.22981.

40. Giesert F, Hofmann A, Bürger A, Zerle J, Kloos K, Hafen U, et al. Expression Analysis of Lrrk1, Lrrk2 and Lrrk2 Splice Variants in Mice. PLoS ONE. 2013;8(5):e63778. doi: 10.1371/journal.pone.0063778. PubMed PMID: PMC3651128.

41. Westerlund M, Belin AC, Anvret A, Bickford P, Olson L, Galter D. Developmental regulation of leucine-rich repeat kinase 1 and 2 expression in the brain and other rodent and human organs: Implications for Parkinson's disease. Neuroscience. 2008;152(2):429-36. Epub 2008/02/15. doi: 10.1016/j.neuroscience.2007.10.062. PubMed PMID: 18272292.

42. Zechel S, Meinhardt A, Unsicker K, von Bohlen Und Halbach O. Expression of leucine-rich-repeat-kinase 2 (LRRK2) during embryonic development. International journal of developmental neuroscience : the official journal of the International Society for Developmental Neuroscience. 2010;28(5):391-9. Epub 2010/04/21. doi: 10.1016/j.ijdevneu.2010.04.002. PubMed PMID: 20403420.

43. Pradhan S, Andreasson K. Commentary: Progressive inflammation as a contributing factor to early development of Parkinson's disease. Experimental neurology. 2013;241:148-55. Epub 2012/12/25. doi: 10.1016/j.expneurol.2012.12.008. PubMed PMID: 23261765.

44. Russo I, Bubacco L, Greggio E. LRRK2 and neuroinflammation: partners in crime in Parkinson's disease? Journal of neuroinflammation. 2014;11:52. Epub 2014/03/25. doi: 10.1186/1742-2094-11-52. PubMed PMID: 24655756; PubMed Central PMCID: PMCPMC3994422.

45. Stanley PL, Steiner S, Havens M, Tramposch KM. Mouse skin inflammation induced by multiple topical applications of 12-O-tetradecanoylphorbol-13-acetate. Skin pharmacology : the official journal of the Skin Pharmacology Society. 1991;4(4):262-71. Epub 1991/01/01. PubMed PMID: 1789987.

46. Sallinen V, Torkko V, Sundvik M, Reenila I, Khrustalyov D, Kaslin J, et al. MPTP and MPP+ target specific aminergic cell populations in larval zebrafish. Journal of neurochemistry. 2009;108(3):719-31. Epub 2008/12/03. doi: 10.1111/j.1471-4159.2008.05793.x. PubMed PMID: 19046410.

47. Chen YC, Priyadarshini M, Panula P. Complementary developmental expression of the two tyrosine hydroxylase transcripts in zebrafish. Histochemistry and cell biology. 2009;132(4):375-81. Epub 2009/07/16. doi: 10.1007/s00418-009-0619-8. PubMed PMID: 19603179.

48. Semenova SA, Chen YC, Zhao X, Rauvala H, Panula P. The tyrosine hydroxylase 2 (TH2) system in zebrafish brain and stress activation of hypothalamic cells. Histochemistry and cell biology. 2014;142(6):619-33. Epub 2014/07/17. doi: 10.1007/s00418-014-1240-z. PubMed PMID: 25028341.

49. Berwick DC, Harvey K. LRRK2: an eminence grise of Wnt-mediated neurogenesis? Frontiers in cellular neuroscience. 2013;7:82. Epub 2013/06/12. doi: 10.3389/fncel.2013.00082. PubMed PMID: 23754980; PubMed Central PMCID: PMCPMC3668263.

50. Winner B, Melrose HL, Zhao C, Hinkle KM, Yue M, Kent C, et al. Adult neurogenesis and neurite outgrowth are impaired in LRRK2 G2019S mice. Neurobiology of disease. 2011;41(3):706-16. Epub 2010/12/21. doi: 10.1016/j.nbd.2010.12.008. PubMed PMID: 21168496; PubMed Central PMCID: PMCPMC3059106.

51. Paus M, Kohl Z, Ben Abdallah NM, Galter D, Gillardon F, Winkler J. Enhanced dendritogenesis and axogenesis in hippocampal neuroblasts of LRRK2 knockout mice. Brain research. 2013;1497:85-100. Epub 2012/12/29. doi: 10.1016/j.brainres.2012.12.024. PubMed PMID: 23270607.

52. Milosevic J, Schwarz SC, Ogunlade V, Meyer AK, Storch A, Schwarz J. Emerging role of LRRK2 in human neural progenitor cell cycle progression, survival and differentiation. Mol Neurodegener. 2009;4:25. Epub 2009/06/16. doi: 10.1186/1750-1326-4-25. PubMed PMID: 19523245; PubMed Central PMCID: PMCPMC2704190.

53. Winkler S, Gscheidel N, Brand M. Mutant generation in vertebrate model organisms by TILLING. Methods in molecular biology (Clifton, NJ). 2011;770:475-504. Epub 2011/08/02. doi: 10.1007/978-1-61779-210-6_19. PubMed PMID: 21805277.

54. Kroehne V, Freudenreich D, Hans S, Kaslin J, Brand M. Regeneration of the adult zebrafish brain from neurogenic radial glia-type progenitors. Development (Cambridge, England). 2011;138(22):4831-41. Epub 2011/10/19. doi: 10.1242/dev.072587. PubMed PMID: 22007133.

55. Kaslin J, Kroehne V, Ganz J, Hans S, Brand M. Distinct roles of neuroepithelial-like and radial glia-like progenitor cells in cerebellar regeneration. Development (Cambridge, England). 2017. Epub 2017/03/16. doi: 10.1242/dev.144907. PubMed PMID: 28289134.

56. Chen H, Zhao EJ, Zhang W, Lu Y, Liu R, Huang X, et al. Meta-analyses on prevalence of selected Parkinson's nonmotor symptoms before and after diagnosis. Translational Neurodegeneration. 2015;4(1):1. doi: 10.1186/2047-9158-4-1. PubMed PMID: PMC4322463.

57. Atashrazm F, Dzamko N. LRRK2 inhibitors and their potential in the treatment of Parkinson's disease: current perspectives. Clinical Pharmacology : Advances and Applications. 2016;8:177-89. doi: 10.2147/CPAA.S102191. PubMed PMID: PMC5076802.

58. Rubio JP, Topp S, Warren L, St Jean PL, Wegmann D, Kessner D, et al. Deep sequencing of the LRRK2 gene in 14,002 individuals reveals evidence of purifying selection and independent origin of the p.Arg1628Pro mutation in Europe. Human Mutation. 2012;33(7):1087-98. doi: 10.1002/humu.22075. PubMed PMID: PMC3370131.

59. Alcalay RN, Mejia-Santana H, Mirelman A, Saunders-Pullman R, Raymond D, Palmese C, et al. Neuropsychological performance in LRRK2 G2019S carriers with Parkinson's disease. Parkinsonism & related disorders. 2015;21(2):106-10. doi: 10.1016/j.parkreldis.2014.09.033. PubMed PMID: PMC4306614.

60. Matta S, Van Kolen K, da Cunha R, van den Bogaart G, Mandemakers W, Miskiewicz K, et al. LRRK2 controls an EndoA phosphorylation cycle in synaptic endocytosis. Neuron. 2012;75(6):1008-21. Epub 2012/09/25. doi: 10.1016/j.neuron.2012.08.022. PubMed PMID: 22998870.

61. Pellicano C, Benincasa D, Pisani V, Buttarelli FR, Giovannelli M, Pontieri FE. Prodromal non-motor symptoms of Parkinson's disease. Neuropsychiatric Disease and Treatment. 2007;3(1):145-52. PubMed PMID: PMC2654529.

62. Arranz AM, Delbroek L, Van Kolen K, Guimarães MR, Mandemakers W, Daneels G, et al. LRRK2 functions in synaptic vesicle endocytosis through a kinase-dependent mechanism. Journal of Cell Science. 2015;128(3):541-52. doi: 10.1242/jcs.158196.

63. Dias V, Junn E, Mouradian MM. The Role of Oxidative Stress in Parkinson's Disease. Journal of Parkinson's disease. 2013;3(4):461-91. doi: 10.3233/JPD-130230. PubMed PMID: PMC4135313.

64. Riederer P, Laux G. MAO-inhibitors in Parkinson's Disease. Experimental Neurobiology. 2011;20(1):1-17. doi: 10.5607/en.2011.20.1.1. PubMed PMID: PMC3213739.

65. Yoles E, Hauben E, Palgi O, Agranov E, Gothilf A, Cohen A, et al. Protective autoimmunity is a physiological response to CNS trauma. J Neurosci. 2001;21(11):3740-8. Epub 2001/05/23. PubMed PMID: 11356861.

66. Kyritsis N, Kizil C, Zocher S, Kroehne V, Kaslin J, Freudenreich D, et al. Acute inflammation initiates the regenerative response in the adult zebrafish brain. Science (New York, NY). 2012;338(6112):1353-6. Epub 2012/11/10. doi: 10.1126/science.1228773. PubMed PMID: 23138980.

67. Ohnmacht J, Yang Y, Maurer GW, Barreiro-Iglesias A, Tsarouchas TM, Wehner D, et al. Spinal motor neurons are regenerated after mechanical lesion and genetic ablation in larval zebrafish. Development (Cambridge, England). 2016;143(9):1464-74. doi: 10.1242/dev.129155. PubMed PMID: PMC4986163.

68. Wright MA, Mo W, Nicolson T, Ribera AB. In vivo evidence for transdifferentiation of peripheral neurons. Development (Cambridge, England). 2010;137(18):3047-56. doi: 10.1242/dev.052696. PubMed PMID: PMC2926955.

69. Moehle MS, Webber PJ, Tse T, Sukar N, Standaert DG, DeSilva TM, et al. LRRK2 inhibition attenuates microglial inflammatory responses. J Neurosci. 2012;32(5):1602-11. Epub 2012/02/04. doi: 10.1523/jneurosci.5601-11.2012. PubMed PMID: 22302802; PubMed Central PMCID: PMCPMC3532034.

70. Choi I, Kim B, Byun J-W, Baik SH, Huh YH, Kim J-H, et al. LRRK2 G2019S mutation attenuates microglial motility by inhibiting focal adhesion kinase. Nature Communications. 2015;6:8255. doi: 10.1038/ncomms9255. PubMed PMID: PMC4647842.

71. Crane PK, Gibbons LE, Dams-O'Connor K, Trittschuh E, Leverenz JB, Keene CD, et al. Association of Traumatic Brain Injury With Late-Life Neurodegenerative Conditions and Neuropathologic Findings. JAMA neurology. 2016;73(9):1062-9. Epub 2016/07/12. doi: 10.1001/jamaneurol.2016.1948. PubMed PMID: 27400367.

72. Sievers F, Wilm A, Dineen D, Gibson TJ, Karplus K, Li W, et al. Fast, scalable generation of high-quality protein multiple sequence alignments using Clustal Omega. Molecular Systems Biology. 2011;7(1). doi: 10.1038/msb.2011.75.

73. Altschul SF, Gish W, Miller W, Myers EW, Lipman DJ. Basic local alignment search tool. Journal of molecular biology. 1990;215(3):403-10. Epub 1990/10/05. doi: 10.1016/s0022-2836(05)80360-2. PubMed PMID: 2231712.

74. Jao LE, Wente SR, Chen W. Efficient multiplex biallelic zebrafish genome editing using a CRISPR nuclease system. Proceedings of the National Academy of Sciences of the United States of America. 2013;110(34):13904-9. Epub 2013/08/07. doi: 10.1073/pnas.1308335110. PubMed PMID: 23918387; PubMed Central PMCID: PMCPMC3752207.

75. Rupp RA, Snider L, Weintraub H. Xenopus embryos regulate the nuclear localization of XMyoD. Genes & development. 1994;8(11):1311-23. Epub 1994/06/01. PubMed PMID: 7926732.

76. Hans S, Kaslin J, Freudenreich D, Brand M. Temporally-controlled site-specific recombination in zebrafish. PloS one. 2009;4(2):e4640. Epub 2009/02/28. doi: 10.1371/journal.pone.0004640. PubMed PMID: 19247481; PubMed Central PMCID: PMCPMC2645673.

77. Brand M, Granato, M., and Nüsslein-Volhard, C. . Keeping and raising zebrafish. In Zebrafish, A Practical Approach. Oxford , Oxford University Press; . 2002:7-37.

78. Kimmel CB, Ballard WW, Kimmel SR, Ullmann B, Schilling TF. Stages of embryonic development of the zebrafish. Developmental Dynamics. 1995;203(3):253-310. doi: 10.1002/aja.1002030302.

79. Kawakami K, Takeda H, Kawakami N, Kobayashi M, Matsuda N, Mishina M. A transposon-mediated gene trap approach identifies developmentally regulated genes in zebrafish. Dev Cell. 2004;7(1):133-44. Epub 2004/07/09. doi: 10.1016/j.devcel.2004.06.005. PubMed PMID: 15239961.

80. Koide T, Miyasaka N, Morimoto K, Asakawa K, Urasaki A, Kawakami K, et al. Olfactory neural circuitry for attraction to amino acids revealed by transposon-mediated gene trap approach in zebrafish. Proceedings of the National Academy of Sciences. 2009;106(24):9884-9. doi: 10.1073/pnas.0900470106.

81. Susaki EA, Tainaka K, Perrin D, Yukinaga H, Kuno A, Ueda HR. Advanced CUBIC protocols for whole-brain and whole-body clearing and imaging. Nat Protocols. 2015;10(11):1709-27. doi: 10.1038/nprot.2015.085

http://www.nature.com/nprot/journal/v10/n11/abs/nprot.2015.085.html-supplementary-information.

82. Rhinn M, Lun K, Amores A, Yan Y-L, Postlethwait JH, Brand M. Cloning, expression and relationship of zebrafish gbx1 and gbx2 genes to Fgf signaling. Mechanisms of Development. 2003;120(8):919-36. doi: http://dx.doi.org/10.1016/S0925-4773(03)00135-7.

83. Grandel H, Kaslin J, Ganz J, Wenzel I, Brand M. Neural stem cells and neurogenesis in the adult zebrafish brain: origin, proliferation dynamics, migration and cell fate. Dev Biol. 2006;295(1):263-77. Epub 2006/05/10. doi: 10.1016/j.ydbio.2006.03.040. PubMed PMID: 16682018.

84. Reifers F, Bohli H, Walsh EC, Crossley PH, Stainier DY, Brand M. Fgf8 is mutated in zebrafish acerebellar (ace) mutants and is required for maintenance of midbrain-hindbrain boundary development and somitogenesis. Development (Cambridge, England). 1998;125(13):2381-95. Epub 1998/06/04. PubMed PMID: 9609821.

85. Munzel EJ, Schaefer K, Obirei B, Kremmer E, Burton EA, Kuscha V, et al. Claudin k is specifically expressed in cells that form myelin during development of the nervous system and regeneration of the optic nerve in adult zebrafish. Glia. 2012;60(2):253-70. Epub 2011/10/25. doi: 10.1002/glia.21260. PubMed PMID: 22020875.

86. Redd MJ, Kelly G, Dunn G, Way M, Martin P. Imaging macrophage chemotaxis in vivo: studies of microtubule function in zebrafish wound inflammation. Cell motility and the cytoskeleton. 2006;63(7):415-22. Epub 2006/05/04. doi: 10.1002/cm.20133. PubMed PMID: 16671106.

87. Chen YC, Semenova S, Rozov S, Sundvik M, Bonkowsky JL, Panula P. A Novel Developmental Role for Dopaminergic Signaling to Specify Hypothalamic Neurotransmitter Identity. J Biol Chem. 2016;291(42):21880-92. Epub 2016/08/20. doi: 10.1074/jbc.M115.697466. PubMed PMID: 27539857; PubMed Central PMCID: PMCPMC5063973.

88. Anichtchik O, Sallinen V, Peitsaro N, Panula P. Distinct structure and activity of monoamine oxidase in the brain of zebrafish (Danio rerio). The Journal of comparative neurology. 2006;498(5):593-610. Epub 2006/08/19. doi: 10.1002/cne.21057. PubMed PMID: 16917825.

89. Schindelin J, Arganda-Carreras I, Frise E, Kaynig V, Longair M, Pietzsch T, et al. Fiji: an open-source platform for biological-image analysis. Nature methods. 2012;9(7):676-82. Epub 2012/06/30. doi: 10.1038/nmeth.2019. PubMed PMID: 22743772; PubMed Central PMCID: PMCPMC3855844.

90. Ollion J, Cochennec J, Loll F, Escude C, Boudier T. TANGO: a generic tool for high-throughput 3D image analysis for studying nuclear organization. Bioinformatics (Oxford, England). 2013;29(14):1840-1. Epub 2013/05/18. doi: 10.1093/bioinformatics/btt276. PubMed PMID: 23681123; PubMed Central PMCID: PMCPMC3702251.

91. Arganda-Carreras I, Fernandez-Gonzalez R, Munoz-Barrutia A, Ortiz-De-Solorzano C. 3D reconstruction of histological sections: Application to mammary gland tissue. Microscopy research and technique. 2010;73(11):1019-29. Epub 2010/03/17. doi: 10.1002/jemt.20829. PubMed PMID: 20232465.

92. R Development Core Team. R: A Language and Environment for Statistical Computing. Vienna, Austria: R Foundation for Statistical Computing; 2015.

93. Rossiter DG, Loza A. Technical Note: Analyzing land cover change with logistic regression in R. Version 2.4 ed2016 14-May-2016. 67 p.

Figures

Figure 1. Homology between the human LRRK2 and the zebrafish Lrrk2 proteins and generation of the zebrafish *lrrk2*^{tud113} allele. (a) Alignment analysis of the whole sequence and the individual domains of human LRRK2 (NP_940980) and zebrafish Lrrk2 (NP_001188385) proteins reveals a high degree of conservation of the catalytic core. The percentages of identity (same residues at the same positions in the alignment) and similarity (identical residues plus conservative substitutions) are indicated. Abbreviations: ANK, ankyrin domain; COR, C-terminal of Ras of complex proteins; LRR, leucine-rich repeat domain. (b) Scheme reproducing the targeting and screening strategy. The *lrrk2* open reading frame (ORF) is highlighted in black; F1, R1: *lrrk2 ORF*-specific primers; F2, R2*: lrrk2 ORF*-flanking primers; ts1 (magenta), ts2 (green): gRNA target sites (ts). (c) gap-PCR analysis of genomic DNA from wild-type (*lrrk2*$^{+}$), heterozygous (*lrrk2*$^{+/tud113}$), and homozygous mutant (*lrrk2*^{tud113}) individuals. F1 and R1 amplify a 289-bp-long product, F2 and R2 a 204-bp-long product. (d) *lrrk2 in situ* hybridization confirming the complete absence of *lrrk2* expression in 22-hpf *lrrk2*^{tud113} embryos.

Figure 2. Initial neurodevelopmental abnormalities are subsequently compensated. (a, b) TUNEL assay to visualize cell death in the brain. Quantification was carried out over the whole brain, subdivided into anterior (telencephalon), middle (diencephalon, mesencephalon), and posterior (rhombencephalon) portions. The number of apoptotic cells in mzLrrk2 brains is increased at 5 dpf (a, a'), but matched wt levels at 10 dpf (b, b'). (c, d) HuC/D immunohistochemistry to label mature neurons and (e, f) acetylated Tubulin immunohistochemistry to mark the axonal network at 5 (c, e) and 10 dpf (d, f) does not reveal overt signs of degeneration in the optic tectum. (g, h) Claudin k immunohistochemistry shows a delay in myelination in the ventral hindbrain at 5 dpf (g) that is later compensated at 10 dpf (h). (a', b') Plots represent means±s.d. Statistical analyses: (a', b') two-tailed Student's *t*-test. Scale bars: (a, b, g, h) 100 μm; (c, d) 50 μm; (e, f) 20 μm.

Figure 3. Microglia/leukocyte cell number and morphology are altered in mzLrrk2 mutants. (a, a', b, b') Quantification of segmented L-Plastin+ cell number in the brain. The number of microglia/leukocytes was reduced in mzLrrk2 brains at 5 dpf (a, a'), but comparable to controls at 10 dpf (b, b'). (c) Principal component analysis of brain microglia/leukocyte morphology. For each animal, the average morphological parameters were considered; standardized data were used. The samples (dots) and the original variables (arrows) are projected on

the 2D plane defined by PC1 and PC2: V1, volume; V2, surface; V3, ramification; V4, average branch length; V5, maximum branch length; V6, largest shortest path. PC1 opposes cell size (V1, V2) and ramification (V3) to branch extension (V4, V5); PC2 represents overall cell complexity (V4, V5, and V6). Within brackets, the percentage of total variance explained. Note the poor separation between mzLrrk2 and wt samples at 10 dpf. (d, d') Reduced leukocyte response in the tail of 10-dpf mzLrrk2 larvae after 2 h exposure to 12-*O*-tetradecanoylphorbol-13-acetate (TPA) to induce systemic acute inflammation. Segmented objects were quantified within a constant 566.79×124.54 μm area caudal to the anus and comprised between the dorsal longitudinal anastomotic vessel and the caudal artery. Sample n are indicated in the graph (d'). (a', b', d') Plots represent means±s.d. Statistical analyses: (a', b') two-tailed Student's *t*-test; (d') one-tailed Student's *t*-test. (a, b, d) Scale bars: 100 μm.

Figure 4. Loss of *lrrk2* causes transient developmental defects of the catecholaminergic system and perturbed amine catabolism in older fish. (a) The zebrafish catecholaminergic (CA) cell populations in the rostro-caudal axis from the olfactory bulb to the *locus cœruleus* as revealed by tyrosine hydroxylase 1 (TH1) immunohistochemistry at 5 dpf. Pop. 1: olfactory bulb; pop. 2: telencephalic complex; pop. 3: preoptic area, *pars anterior*; pop. 4: preoptic area, *pars posterior*; pop. 5, 6, 11: diencephalic complex; pop. 7: pretectal area; pop. 8: paraventricular organ, *pars anterior*; pop. 9: paraventricular organ, *pars intermedia*; pop. 10: paraventricular organ, *pars posterior*; pop. 12: posterior tuberal nucleus/posterior tuberculum; pop. 13: hypothalamic complex; pop. 14: *locus cœruleus*. (a') Combination of the anti-TH1 antibody with the pan-TH antibody allows the identification of TH2+ cells (white arrowheads) by exclusion. TH2+ cells are found within the TH1 pop. 8, 9, and 10 in the paraventricular organ, thereby constituting the TH2 pop. 8b, 9b, 10b. (b) Simplified scheme of the catabolism of dopamine and serotonin. Each arrow represents a distinct enzymatically-catalyzed step. Grey arrows indicate reactions catalyzed by the combined action of monoamine oxidase/aldehyde dehydrogenase. Abbreviations: 3-MT, 3-methoxytyramine; 5-HIAA, 5-hydroxyindoleacetic acid; 5-HT, serotonin; AD, adrenalin; DA, dopamine; DOPA, 3,4-dihydroxyphenylacetic acid; HVA, homovanillic acid; NA, noradrenalin. (c–h) Quantification of TH1+ (c, e) and TH2+ cells (c', e') in the brain, quantification of amine catabolites in whole larvae (d, f), and histochemical visualization of monoamine oxidase activity in the brain (g, h) at 5 dpf (c–d, g) and 10 dpf (e–f, h). Early defects in discrete CA cell populations at 5 dpf are resolved by 10 dpf. The dopamine catabolism is normal at both time points. (i) Quantification of TH1/2+ cells in 6-mo brains and (j) quantification of TH1 protein levels in 11-mo brains show intact CA system in adult fish. (j') Total protein stain as loading control for the immunoblot in (j). (k) Analysis of amine catabolism in 11-

mo brains reveals increased dopamine and serotonin degradation. (c–f, i, k) Plots represent means±s.d. (j) Protein levels are reported as means±s.d. Statistical analyses: (c pop. 2–14, c', d DA–HVA, d 5-HT, d 5-HIAA, e pop. 1, e 3–14, e', f DA–HVA, f 5-HIAA, i pop.1, i pop. 3–11, i pop. 13, i pop. 14, j, k DA, k DOPAC–5-HIAA) two-tailed Student's *t*-test; (c pop. 1, d 3-MT, e pop. 2, f 5-HT, i pop. 2, i pop. 12) two-tailed Mann-Whitney's *U*-test. (a, g, h) Scale bars: 100 μm.

Figure 5. Loss of *lrrk2* results in reduced mitosis in the larval brain. (a, b) Phospho-histone H3 (pH3) immunohistochemistry to label mitotic cells. The mitosis rate is slightly reduced in the anterior portion only at 5 dpf (a, a'), halved over the whole organ at 10 dpf (b, b'). (c) BrdU immunohistochemistry to label cells in the S phase of the cell cycle. To this aim, a 30 min BrdU pulse was delivered prior to killing. No significant difference between mzLrrk2 and controls was apparent. (d) Combination of the *lrrk2*^{tud113} and *lrrk2*^{tud112} alleles recapitulates the hypoproliferative phenotype in 10-dpf maternal-zygotic tud113 brains. (e, e') Conditional expression of a Lrrk2 fragment (wt+rescue, mzLrrk2+rescue) containing the catalytic core rescues the hypoproliferative phenotype in 10-dpf mzLrrk2 brains (mzLrrk2+rescue versus mzLrrk2 controls, ctrl). (a', b', c, d, e') Plots represent means±s.d. Statistical analyses: (a', b', c anterior, c middle) two-tailed Student's *t*-test; (c posterior) two-tailed Mann-Whitney's *U*-test; (d) one-way ANOVA followed by Tukey's *post hoc* test; (e') one-way ANOVA followed by Dunn-Šidák's correction for multiple comparisons. Multiple comparisons: (e') wt ctrl vs. wt+rescue; wt ctrl vs. mzLrrk2 ctrl; wt ctrl vs. mzLrrk2+rescue; mzLrrk2 ctrl vs. mzLrrk2+rescue. Scale bars: (a, b, e) 100 μm.

Figure 6. Loss of *lrrk2* impairs neuronal regeneration upon stab injury of adult telencephalon. (a) A unilateral stab injury was inflicted to the 6-mo adult telencephalon. To identify newborn neurons, a BrdU pulse was delivered from 2 to 3 days post-lesion (dpl) and incorporating cells analyzed at 21 dpl. (b) PCNA immunohistochemistry to examine reactive proliferation in radial glia stem cells of the ventricular zone (VZ) at 3 dpl. The lesioned hemisphere (3 dpl) was compared to the unlesioned hemisphere as control (ctrl) but no difference was observed (c, c'). HuC/D/BrdU double labeling to assess neurogenesis at 21 dpl. Double-positive cells are indicated by white arrowheads in the insets. Quantification was carried out through the entire parenchyma of the lesioned (21 dpl) and ctrl hemispheres. Neurogenesis is reduced in the mzLrrk2 brains. Orange-boxed insets are rotated by 90°. (b, c') Plots represent means±s.d. Statistical analyses: one-tailed Student's *t*-test. (c) Scale bar: 50 μm.

Figure 7. Overview of the main findings.

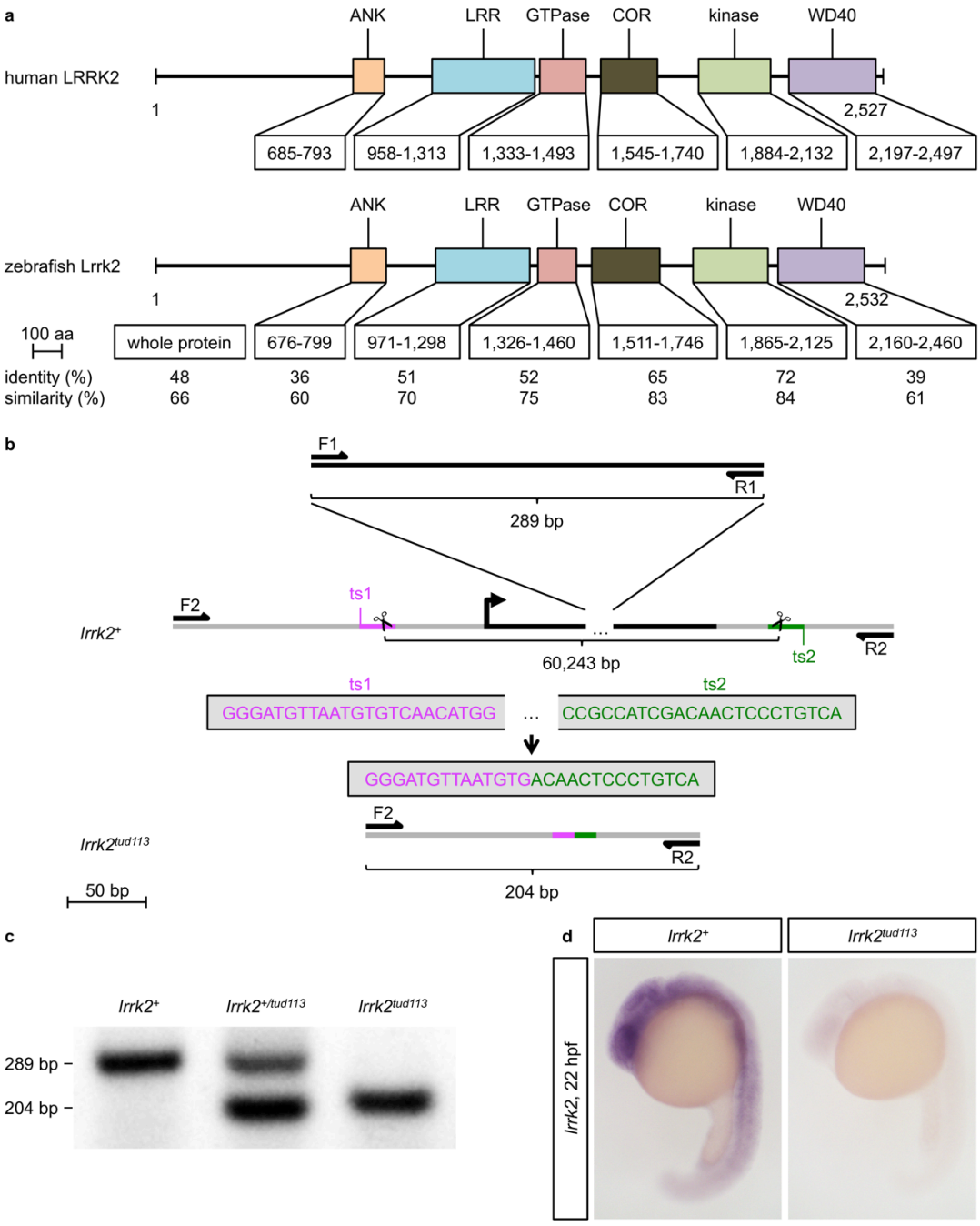
a
ANK
LRR
GTPase
COR
kinase
WD40
human LRRK2
1
2,527
685-793
958-1,313
1,333-1,493
1,545-1,740
1,884-2,132
2,197-2,497
zebrafish Lrrk2
1
2,532
100 aa
whole protein
676-799
971-1,298
1,326-1,460
1,511-1,746
1,865-2,125
2,160-2,460
identity (%) 48 36 51 52 65 72 39
similarity (%) 66 60 70 75 83 84 61
b
F1
R1
289 bp
F2
ts1
lrrk2+
60,243 bp
ts2
R2
GGGATGTTAATGTGTCAACATGG
CCGCCATCGACAACTCCCTGTCA
GGGATGTTAATGTGACAACTCCCTGTCA
lrrk2tud113
50 bp
204 bp
c
lrrk2+
lrrk2+/tud113
lrrk2tud113
289 bp
204 bp
d
lrrk2+
lrrk2tud113
lrrk2, 22 hpf

Figure 1

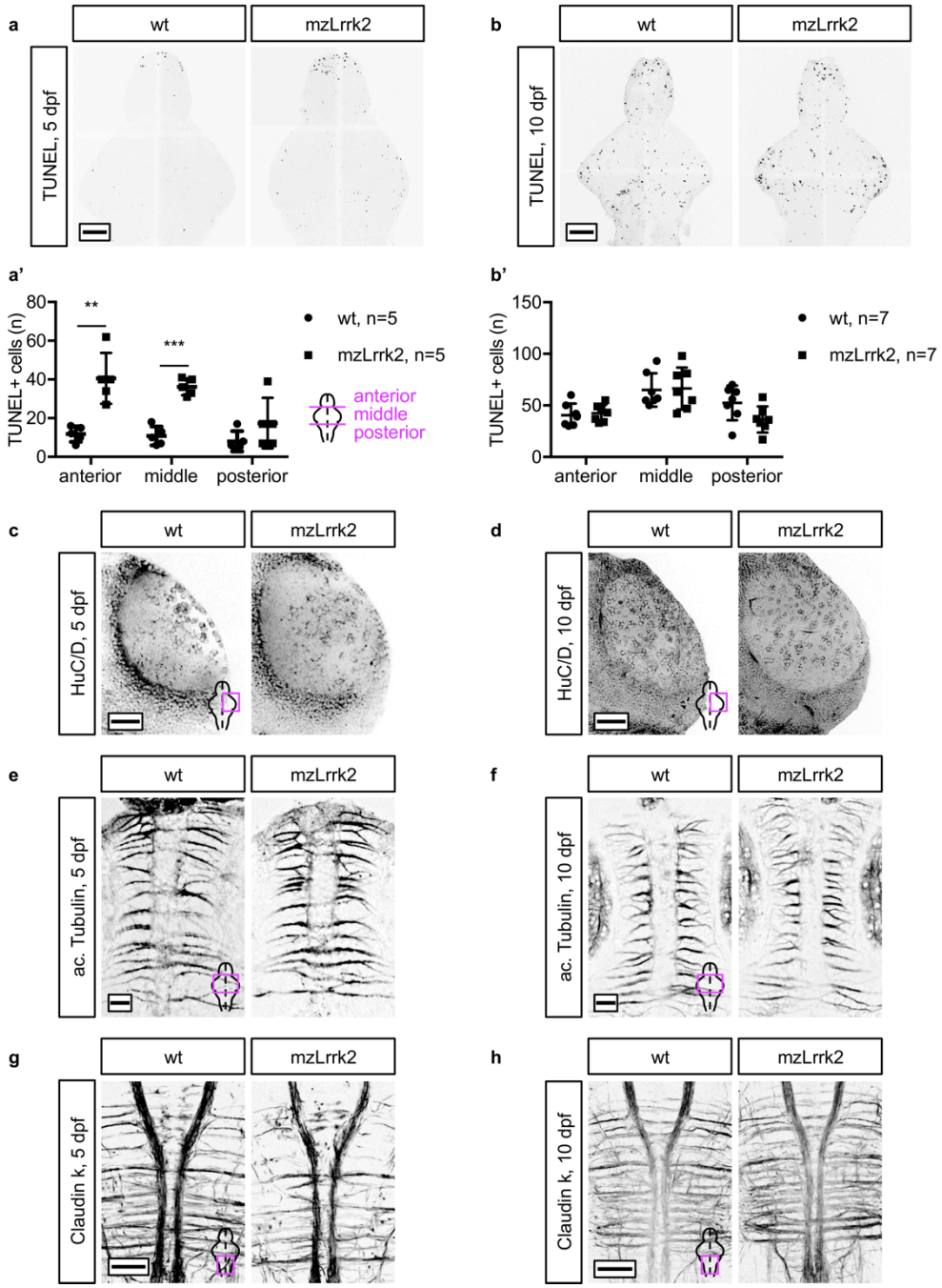
a
wt
mzLrrk2
TUNEL, 5 dpf
b
wt
mzLrrk2
TUNEL, 10 dpf
a'
TUNEL+ cells (n)
80
60
40
20
0
**
***
anterior
middle
posterior
wt, n=5
mzLrrk2, n=5
anterior
middle
posterior
b'
TUNEL+ cells (n)
150
100
50
0
anterior
middle
posterior
wt, n=7
mzLrrk2, n=7
c
wt
mzLrrk2
HuC/D, 5 dpf
d
wt
mzLrrk2
HuC/D, 10 dpf
e
wt
mzLrrk2
ac. Tubulin, 5 dpf
f
wt
mzLrrk2
ac. Tubulin, 10 dpf
g
wt
mzLrrk2
Claudin k, 5 dpf
h
wt
mzLrrk2
Claudin k, 10 dpf

Figure 2

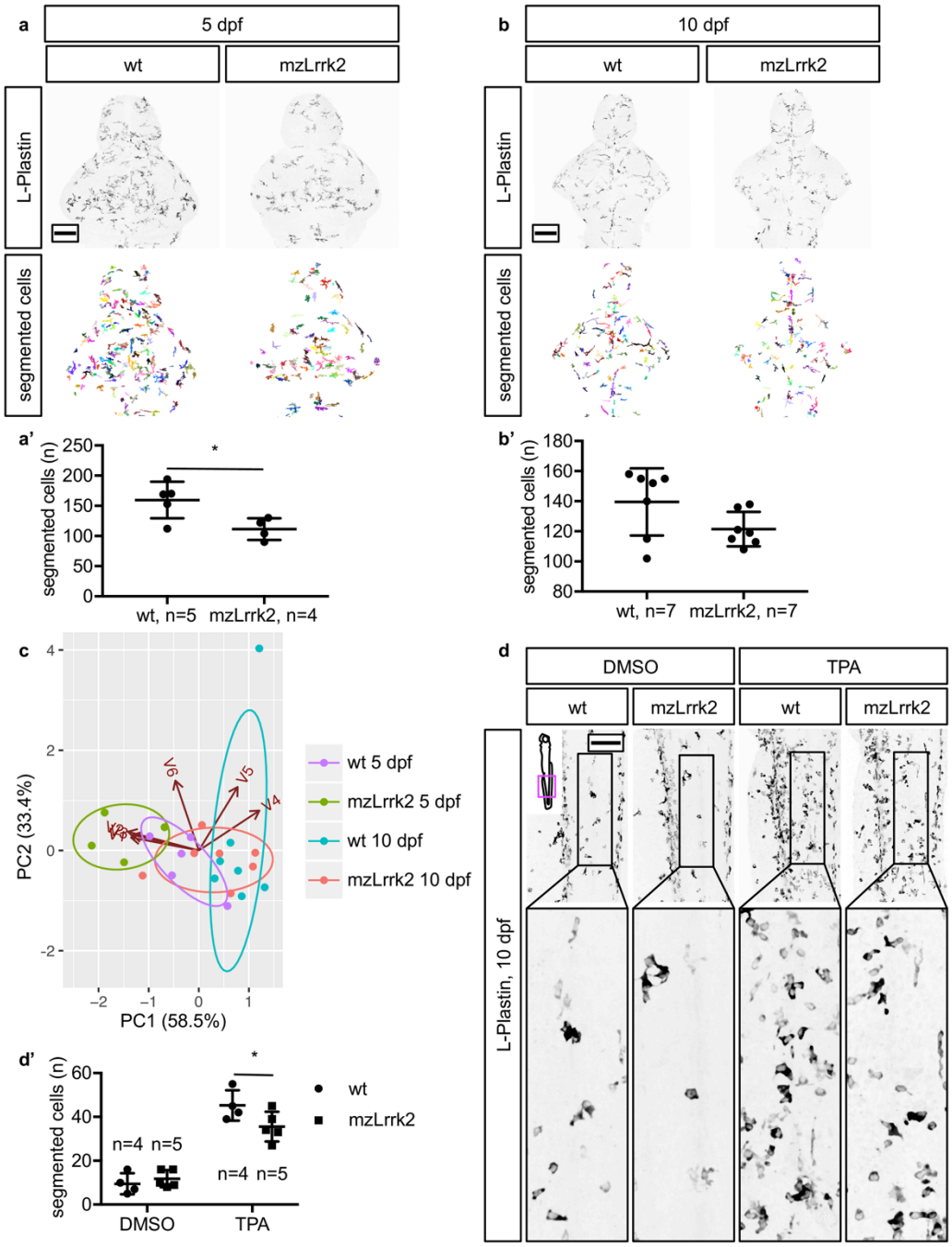
a
5 dpf
wt
mzLrrk2
L-Plastin
segmented cells
b
10 dpf
wt
mzLrrk2
L-Plastin
segmented cells
a'
segmented cells (n)
250
200
150
100
50
0
*
wt, n=5
mzLrrk2, n=4
b'
segmented cells (n)
180
160
140
120
100
80
wt, n=7
mzLrrk2, n=7
c
PC2 (33.4%)
PC1 (58.5%)
V6
V5
V4
wt 5 dpf
mzLrrk2 5 dpf
wt 10 dpf
mzLrrk2 10 dpf
d'
segmented cells (n)
60
40
20
0
n=4 n=5
n=4 n=5
*
DMSO
TPA
wt
mzLrrk2
d
DMSO
TPA
wt
mzLrrk2
wt
mzLrrk2
L-Plastin, 10 dpf

Figure 3

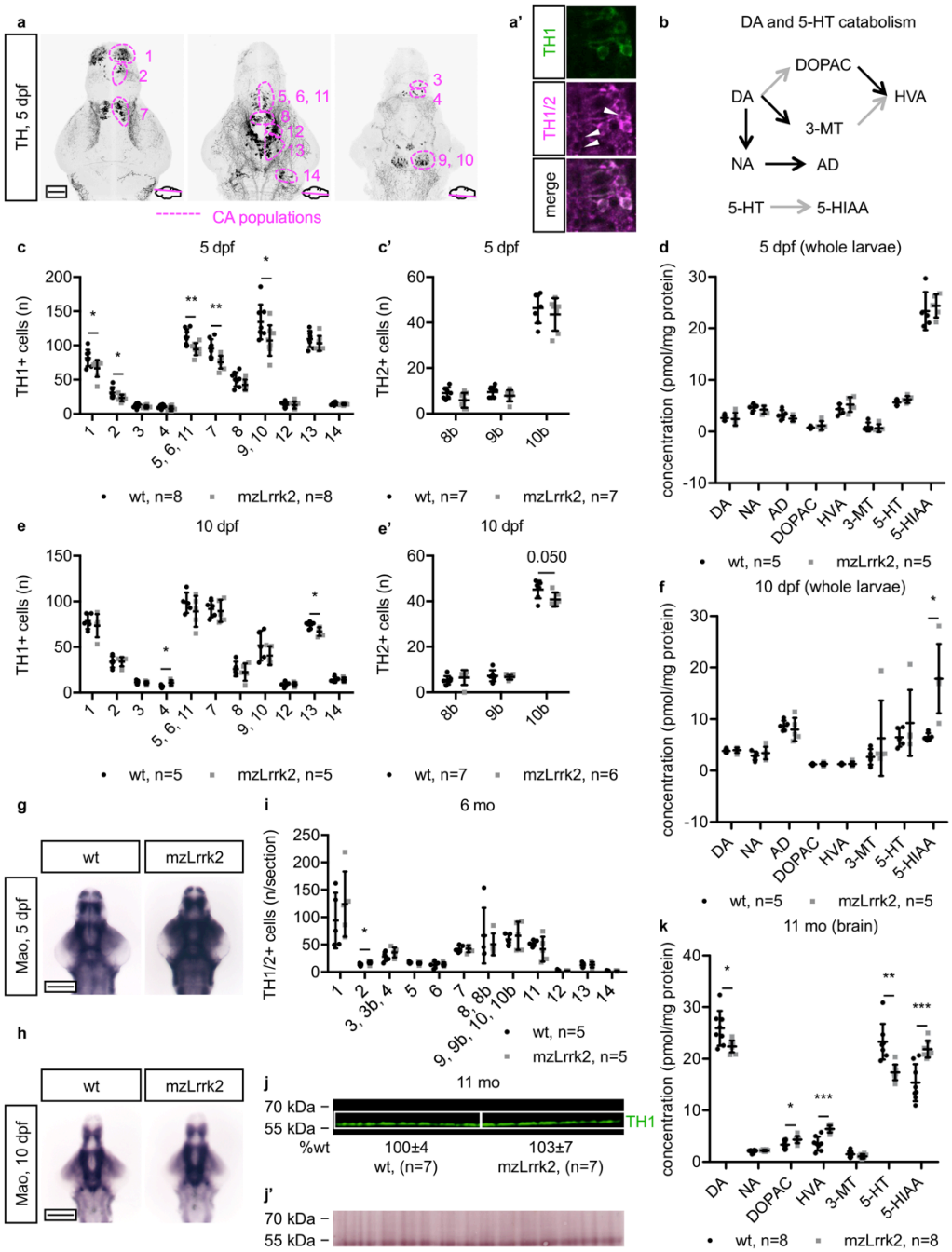
a
TH, 5 dpf
CA populations
a'
TH1
TH1/2
merge
b
DA and 5-HT catabolism
DOPAC
DA
HVA
3-MT
NA
AD
5-HT
5-HIAA
c
5 dpf
TH1+ cells (n)
wt, n=8
mzLrrk2, n=8
c'
5 dpf
TH2+ cells (n)
wt, n=7
mzLrrk2, n=7
d
5 dpf (whole larvae)
concentration (pmol/mg protein)
wt, n=5
mzLrrk2, n=5
e
10 dpf
TH1+ cells (n)
wt, n=5
mzLrrk2, n=5
e'
10 dpf
TH2+ cells (n)
0.050
wt, n=7
mzLrrk2, n=6
f
10 dpf (whole larvae)
concentration (pmol/mg protein)
wt, n=5
mzLrrk2, n=5
g
wt
mzLrrk2
Mao, 5 dpf
h
wt
mzLrrk2
Mao, 10 dpf
i
6 mo
TH1/2+ cells (n/section)
wt, n=5
mzLrrk2, n=5
j
11 mo
70 kDa
55 kDa
TH1
%wt
100±4
wt, (n=7)
103±7
mzLrrk2, (n=7)
j'
70 kDa
55 kDa
k
11 mo (brain)
concentration (pmol/mg protein)
wt, n=8
mzLrrk2, n=8

Figure 4

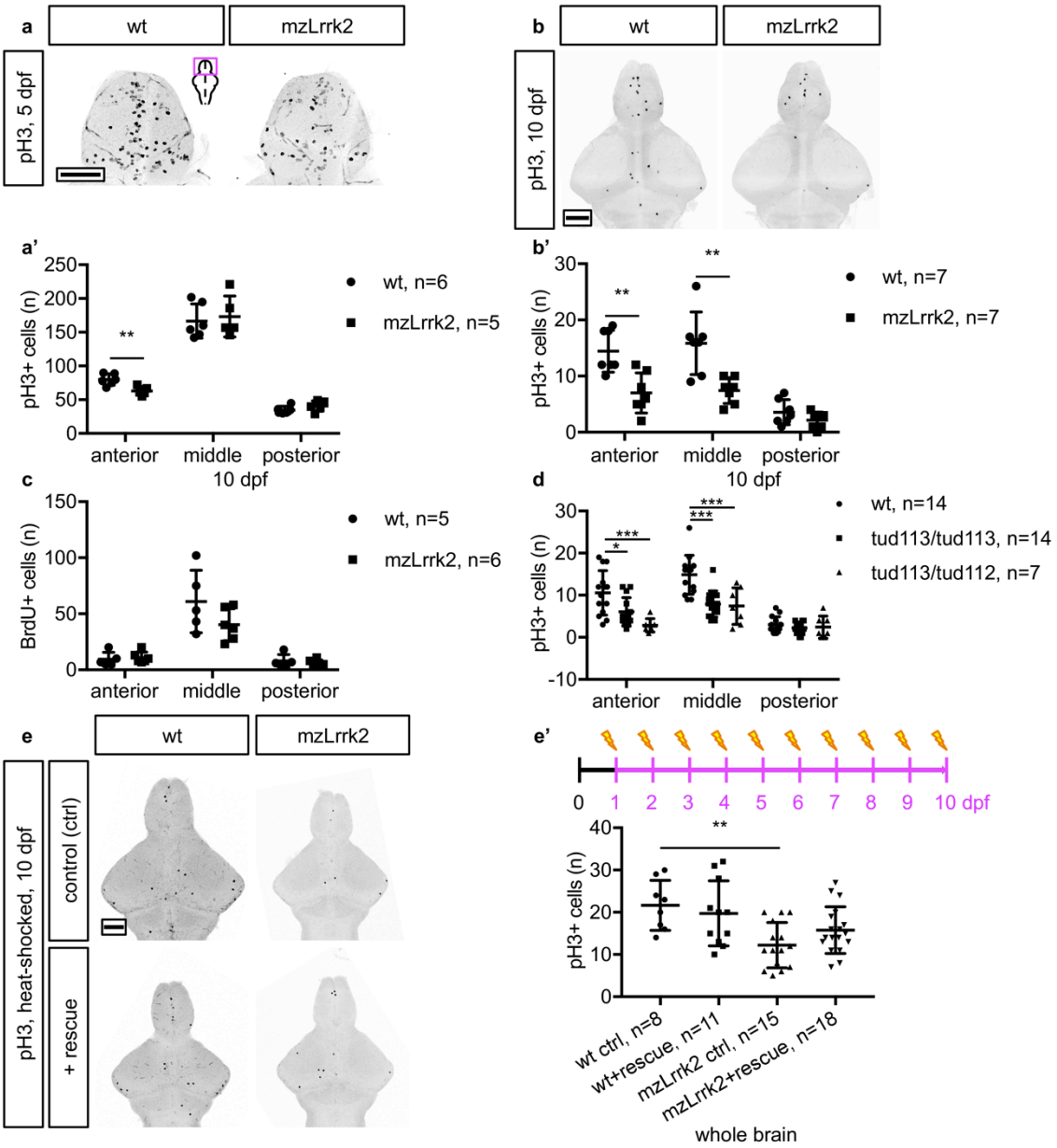
a
wt
mzLrrk2
pH3, 5 dpf
b
wt
mzLrrk2
pH3, 10 dpf
a'
pH3+ cells (n)
wt, n=6
mzLrrk2, n=5
anterior
middle
posterior
10 dpf
b'
pH3+ cells (n)
wt, n=7
mzLrrk2, n=7
c
BrdU+ cells (n)
wt, n=5
mzLrrk2, n=6
d
pH3+ cells (n)
wt, n=14
tud113/tud113, n=14
tud113/tud112, n=7
e
wt
mzLrrk2
pH3, heat-shocked, 10 dpf
control (ctrl)
+ rescue
e'
0 1 2 3 4 5 6 7 8 9 10 dpf
pH3+ cells (n)
wt ctrl, n=8
wt+rescue, n=11
mzLrrk2 ctrl, n=15
mzLrrk2+rescue, n=18
whole brain

Figure 5

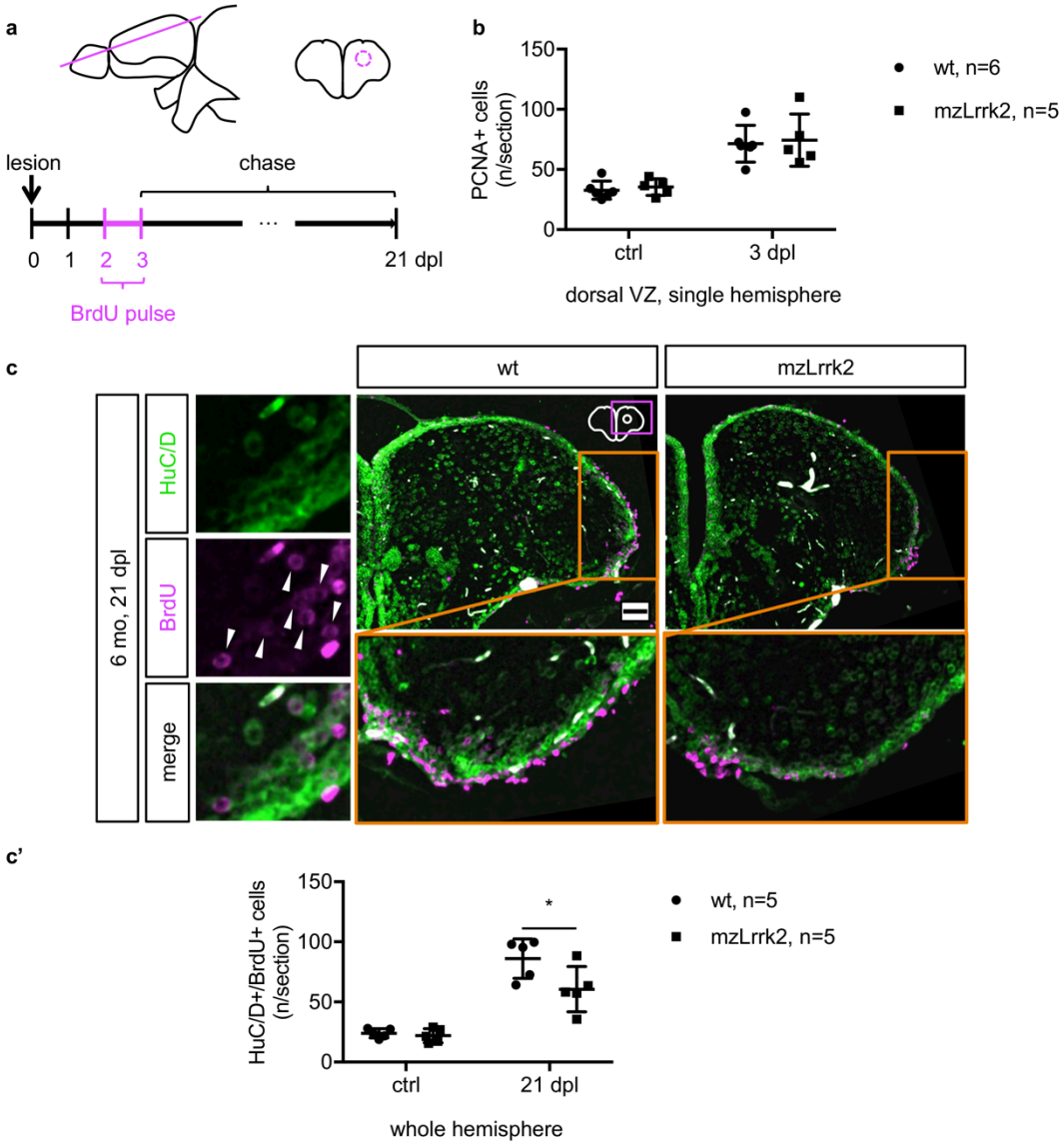
a
lesion
chase
0
1
2
3
21 dpl
BrdU pulse
b
PCNA+ cells (n/section)
150
100
50
0
ctrl
3 dpl
dorsal VZ, single hemisphere
wt, n=6
mzLrrk2, n=5
c
wt
mzLrrk2
6 mo, 21 dpl
HuC/D
BrdU
merge
c'
HuC/D+/BrdU+ cells (n/section)
150
100
50
0
*
ctrl
21 dpl
whole hemisphere
wt, n=5
mzLrrk2, n=5

Figure 6

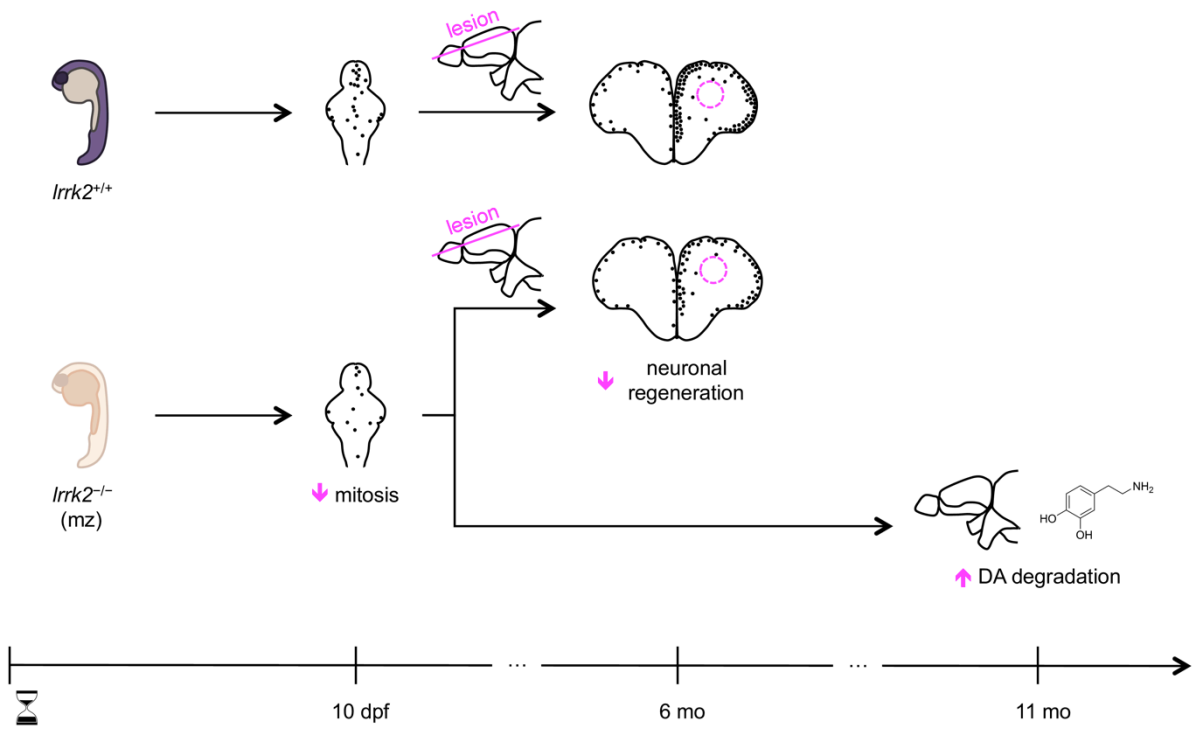
lesion
lrrk2+/+
lesion
neuronal
regeneration
lrrk2−/−
(mz)
mitosis
NH2
HO
OH
DA degradation
10 dpf
6 mo
11 mo

Figure 7